



Review

# Research Progress on Graphite-Derived Materials for Electrocatalysis in Energy Conversion and Storage

Shuaijie He <sup>1,2,3</sup>, Mingjie Wu <sup>4,5,\*</sup>, Song Li <sup>1,2</sup>, Zhiyi Jiang <sup>1,2</sup>, Hanlie Hong <sup>1,3</sup>, Sylvain G. Cloutier <sup>6</sup>, Huaming Yang <sup>1,2,7,\*</sup> , Sasha Omanovic <sup>4,\*</sup> , Shuhui Sun <sup>5</sup> and Gaixia Zhang <sup>6,\*</sup>

- <sup>1</sup> Engineering Research Center of Nano-Geomaterials of Ministry of Education, China University of Geosciences, Wuhan 430074, China
- <sup>2</sup> Faculty of Materials Science and Chemistry, China University of Geosciences, Wuhan 430074, China
- <sup>3</sup> School of Earth Sciences, China University of Geosciences, Wuhan 430074, China
- <sup>4</sup> Department of Chemical Engineering, McGill University, 3610 University Street, Montreal, QC H3A 0C5, Canada
- <sup>5</sup> Institut National de la Recherche Scientifique (INRS), Centre Énergie Matériaux Télécommunications, Varennes, QC J3X 1P7, Canada
- <sup>6</sup> Department of Electrical Engineering, École de Technologie Supérieure (ÉTS), Montreal, QC H3C 1K3, Canada
- <sup>7</sup> Hunan Key Laboratory of Mineral Materials and Application, School of Minerals Processing and Bioengineering, Central South University, Changsha 410083, China
- \* Correspondence: mingjie.wu@mail.mcgill.ca (M.W.); hm.yang@cug.edu.cn (H.Y.); sasha.omanovic@mcgill.ca (S.O.); gaixia.zhang@etsmtl.ca (G.Z.)



**Citation:** He, S.; Wu, M.; Li, S.; Jiang, Z.; Hong, H.; Cloutier, S.G.; Yang, H.; Omanovic, S.; Sun, S.; Zhang, G. Research Progress on Graphite-Derived Materials for Electrocatalysis in Energy Conversion and Storage. *Molecules* **2022**, *27*, 8644. <https://doi.org/10.3390/molecules27248644>

Academic Editor: Munkhbayar Batmunkh

Received: 12 November 2022

Accepted: 5 December 2022

Published: 7 December 2022

**Publisher's Note:** MDPI stays neutral with regard to jurisdictional claims in published maps and institutional affiliations.



**Copyright:** © 2022 by the authors. Licensee MDPI, Basel, Switzerland. This article is an open access article distributed under the terms and conditions of the Creative Commons Attribution (CC BY) license (<https://creativecommons.org/licenses/by/4.0/>).

**Abstract:** High-performance electrocatalysts are critical to support emerging electrochemical energy storage and conversion technologies. Graphite-derived materials, including fullerenes, carbon nanotubes, and graphene, have been recognized as promising electrocatalysts and electrocatalyst supports for the oxygen reduction reaction (ORR), oxygen evolution reaction (OER), hydrogen evolution reaction (HER), and carbon dioxide reduction reaction (CO<sub>2</sub>RR). Effective modification/functionalization of graphite-derived materials can promote higher electrocatalytic activity, stability, and durability. In this review, the mechanisms and evaluation parameters for the above-outlined electrochemical reactions are introduced first. Then, we emphasize the preparation methods for graphite-derived materials and modification strategies. We further highlight the importance of the structural changes of modified graphite-derived materials on electrocatalytic activity and stability. Finally, future directions and perspectives towards new and better graphite-derived materials are presented.

**Keywords:** graphite-derived materials; fullerenes; carbon nanotubes; graphene; electrocatalysis

## 1. Introduction

The sustainable development of green and clean energy systems is one of the most complex problems facing human society. The vigorous development of electrochemical energy storage and conversion systems, such as new metal-air cells, fuel cells, water splitting, and carbon dioxide reduction, has pointed out a new direction for solving world energy problems. However, the slow reaction in core electrochemical reactions, including the oxygen reduction reaction (ORR), oxygen evolution reaction (OER), hydrogen evolution reaction (HER), and carbon dioxide reduction reaction (CO<sub>2</sub>RR), have become the bottleneck restricting the development of new energy technologies. Noble metal materials like platinum (Pt), iridium (Ir), and ruthenium (Ru) have been found to be the most efficient and selective electrocatalysts [1–3]. However, the limited reserves and the poor selectivity of these noble metals gravely impede practical applications of the technologies [4,5]. Carbon materials are promising substitutes for noble-metal-based electrocatalysts due to their abundant resources and easy modification. Among them, graphite-derived materials (fullerene, carbon nanotubes, and graphene) have attracted much attention owing to magnificent characteristics, such as high surface area, electron carrier mobility, and excellent

catalytic activity [6–8]. This review intends to summarize recent progress in emerging electrocatalysts based on graphite-derived materials (Figure 1). Moreover, we discuss various means to boost electrocatalytic performance based on summarizing the structures and properties of different graphite-derived materials. Besides, the challenges and outlooks in this field are also presented to clarify the current situation of the reconstruction strategy of graphite-derived materials and the rational designs of high-performance electrocatalysts.

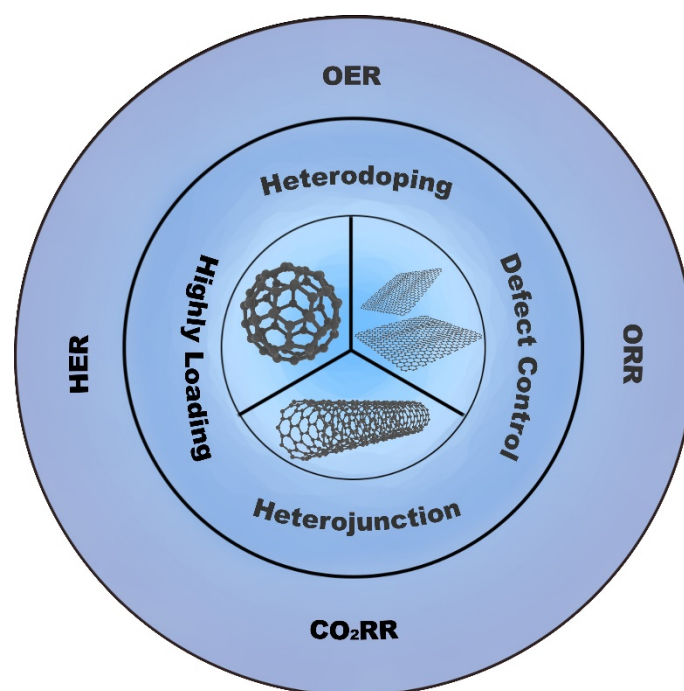


**Figure 1.** Graphite-derived materials and modification approaches used to develop advanced electrocatalysts for electrochemical energy storage and conversion systems based on the four redox reactions depicted in the figure.

## 2. Overview of Electrocatalysis

Electrocatalysis with high catalytic activity and superior durability is required to achieve high power density and stability for electrochemical energy storage and conversion devices. Nevertheless, the core electrochemical reactions, such as ORR, OER, HER, and CO<sub>2</sub>RR, have high overpotential, and slow electron transfer dynamics, which has dramatically hindered the development of electrocatalysis [9–11]. Therefore, the use of highly active and selective catalysts to overcome the kinetics barriers related to the multi-step electron transfer process characterizing these reactions plays a pivotal role in electrocatalysis [12,13].

Electrochemical water splitting is a green, environmentally friendly, and efficient way to produce hydrogen, which involves two reactions: OER and HER. Among them, HER involves a double-electron transfer process, including the adsorption of water molecules or protons on the active site on the electrocatalyst surface (the Volmer step) and the desorption of hydrogen molecules from the cathode through the Tafel or Heyrovsky pathway (Figure 2a) [8,14,15]. Compared with HER, the OER involves a complex four-electron-proton transfer process and multiple reaction intermediates (Figure 2b), resulting in slower kinetics and higher overpotentials. OER restricts water-splitting development and is a significant constraint for new energy technologies such as regenerative fuel cells and rechargeable metal-air batteries [8,16–19].

The ORR reaction processes can generally be divided into two types: the four-electron (4-e<sup>-</sup>) reduction pathway, which directly transports oxygen to produce water; and the two-electron (2-e<sup>-</sup>) reduction pathway, which involves the conversion of oxygen to hydrogen peroxide and then to water (Figure 2c) [8]. The slow reaction kinetics of the ORR hinder

the development of fuel cells and metal-air batteries [8,20–22]. Pt plays a significant role in ORR catalysis [23].

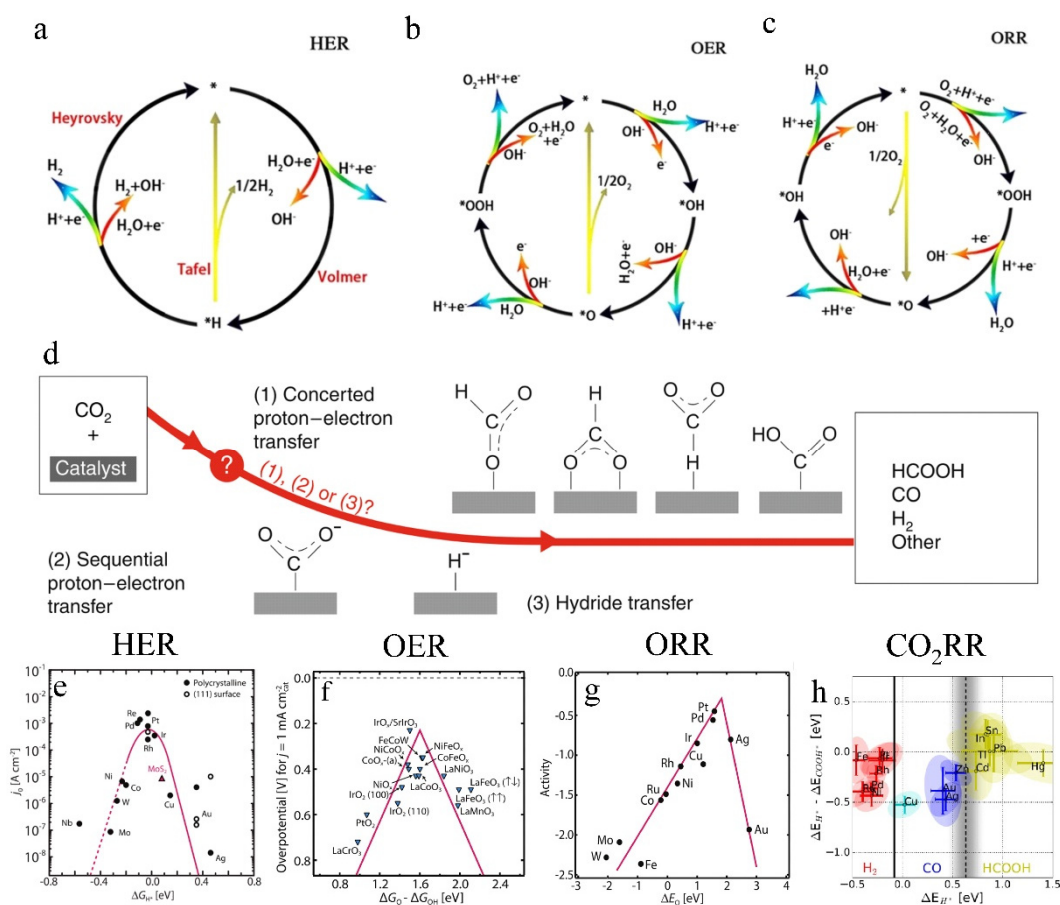


**Figure 2.** (a) HER mechanism in acid (blue line) and alkaline (red line) electrolytes. (b) OER mechanism in acid (blue line) and alkaline (red line) electrolytes. (c) ORR mechanism in acid (blue line) and alkaline (red line) electrolytes. Reproduced with permission [8]. Copyright 2020, Elsevier Ltd., Amsterdam, Netherlands. (d) CO<sub>2</sub>RR mechanism. Reproduced with permission [24]. Copyright 2019, Nature Publishing Group. (e) HER volcano plot for metals and MoS<sub>2</sub>. (f) OER volcano plot for metal oxides. (g) ORR volcano plot for metals. Reproduced with permission [17]. Copyright 2017, American Association for the Advancement of Science. (h) CO<sub>2</sub> reduction metal classification. Reproduced with permission [25]. Copyright 2017, Wiley-VCH Verlag GmbH & Co. KGaA, Weinheim, Germany.

The CO<sub>2</sub>RR reaction mainly consists of three steps: chemisorption of CO<sub>2</sub> from the electrolyte to the catalyst surface, electron or proton transfer to break C–O bonds and form C–H bonds, and product desorption from the catalyst surface (Figure 2d) [24,25]. This reaction provides a clean, sustainable route for producing high-value-added fuels and chemical precursors [26]. However, factors such as the chemical inertness of CO<sub>2</sub>, the reaction competition between HER and CO<sub>2</sub>RR, and the complex intermediates generated by the multiproton and electron reaction process lead to sluggish CO<sub>2</sub>RR kinetics [24,27,28]. Meanwhile, Cu-based materials are considered the only heterogeneous catalysts that promote the formation of various byproducts (e.g., hydrocarbon products and oxygenates) from the CO<sub>2</sub>RR [29].

Efficient catalysts can effectively reduce reaction barriers, promote the conversion of reaction intermediates, and accelerate reaction kinetics [30]. Therefore, developing highly active catalysts has become the top priority in developing the above-mentioned electrochemistry-based energy conversion and storage systems. The electrocatalytic activity largely depends on the binding energy between the reaction intermediates and the catalyst

surface. Empirically, the bond strength between the catalyst and reaction intermediates is neither too strong nor too weak, which is shown by the volcano trends (Figure 2e–h) that can be used to evaluate the intrinsic activity of the electrocatalyst [17,25].

To comprehensively evaluate the catalytic activity of catalysts in the ORR, OER, HER, and CO<sub>2</sub>RR, the following standardized parameters will be considered further in the text: including overpotential ( $\eta_X$ , X represents current density), onset overpotential ( $E_{\text{onset}}$ ), half-wave potential ( $E_{1/2}$ ), electrochemical impedance spectroscopy (EIS), electrochemical active surface area (ECSA), turnover frequency (TOF), faradaic efficiency (FE), current density, limiting current density, Tafel slope, and stability.

### 3. Research Status on Graphite-Derived Materials

The graphite-derived materials such as fullerenes, carbon nanotubes, and graphene are widely used in the preparation of electrochemical catalysts due to their high specific surface area, environmental friendliness, excellent electrical properties, and the easiness of their surface functionalization.

Graphite, which is listed as a strategic mineral for crucial development and protection by some countries [31], is widely used in electrocatalysis [32], environmental protection [33], energy storage [34], refractories [31], thermal management [35], and many other industries. It has become an indispensable non-metallic material for many new strategic sectors. Fullerenes, carbon nanotubes, graphene, and other graphite-derived materials further broaden the application space of graphite in electrocatalysis.

Since Kroto discovered fullerene (C<sub>60</sub>) for the first time in the experiment of laser irradiation and evaporation of graphite, he then successively discovered fullerene molecules such as C<sub>70</sub>, C<sub>80</sub>, and C<sub>90</sub>. C<sub>60</sub>, which have high stability and ideal spherical structure. These fullerene molecules are considered the most representative zero-dimensional carbon material [36]. Due to the highly degenerate molecular energy level and small energy range, C<sub>60</sub> has a high electronic affinity and solid chemical activity. It is often used as an electron acceptor to construct composite functional materials [37]. Currently, the main preparation methods of fullerenes include the laser, arc, and chemical synthesis methods [38].

Iijima of NEC in Japan accidentally discovered carbon nanotubes while preparing carbon fibers [39]. Carbon nanotubes can be divided into armchair-type carbon nanotubes, sawtooth-type carbon nanotubes, and chiral-type carbon nanotubes according to different crimping directions of graphene [40,41]. Based on the different layers of graphene, carbon nanotubes can be named single-walled carbon nanotubes (SWCNTs), double-walled carbon nanotubes (DWCNTs), and multi-walled carbon nanotubes (MWCNTs) (Figure 3a). Currently, arc-discharge, laser ablation, and chemical vapor deposition (CVD) are commonly used to prepare carbon nanotubes (Figure 3b) [42]. The tubes as carriers are characterized by high electrical conductivity, large specific surface area, and adjustable surface [43], which can greatly improve the conductivity of supported catalysts [44,45].

Graphene was successfully obtained by the research group of Professor Geim through mechanical stripping [46]. Graphene, as a two-dimensional carbon material, is composed of carbon atoms with sp<sup>2</sup> hybrid orbital in a hexagonal honeycomb arrangement, which can be divided into a single-layer, double-layer, few-layers (3–10 layers) and multi-layer graphene (more than 10 layers, and less than 10 nm). Because of its good mechanical properties, extremely high carriers (electrons and holes) migration speed, superior electrical conductivity, and huge specific surface area [47,48], the star material has aroused great attention in many fields [49]. The existing preparation methods for graphene mainly include mechanical liquid phase, electrochemical, (CVD), and oxidation-reduction methods, which allow the synthesis of a wide range of graphene in terms of size, quality, and price for any particular application (Figure 3c) [50,51]. The zero-dimensional (0D) fullerenes, one-dimensional (1D) carbon nanotubes, and two-dimensional (2D) graphene constitute a family of graphite-derived materials (Figure 3d). Graphite is composed of multilayer graphene with weak van der Waals force. Carbon nanotubes can be regarded as graphene sheets rolled, which is attributed to the sp<sup>2</sup> hybridization of carbon atoms and part of the sp<sup>3</sup>

hybridization. Fullerenes are made by bending graphene into balls. Therefore, graphene is the basic structural unit of various carbon  $sp^2$  hybrids materials such as fullerenes, carbon nanotubes, and graphite. Furthermore, graphite-derived materials that can be compounded with each other can improve the specific surface area, electron mobility, and energy band structure, thereby effectively improving the electrocatalytic activity [52].

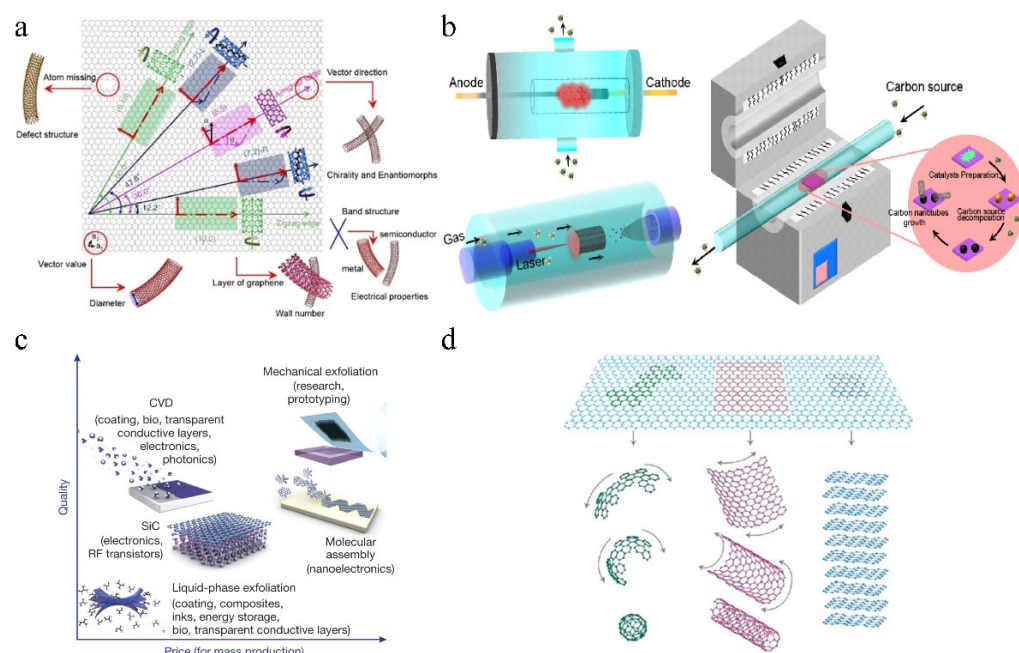


**Figure 3.** (a) Classification of carbon nanotubes (CNTs). (b) Techniques employed for the synthesis of CNT. Reproduced with permission [42]. Copyright 2020, China Academic Journal Electronic Publishing House. (c) Methods of mas-production of graphene. Reproduced with permission [50]. Copyright 2012, Nature Publishing Group. (d) Schematic diagram of graphene as a building unit to form fullerene, carbon nanotubes, and graphite. Reproduced with permission [52]. Copyright 2007, Nature Publishing Group.

## 4. Research Status on Fullerenes in Electrocatalysis

### 4.1. Doped Fullerene

Heteroatom doping can change the intrinsic electronic properties, atomic spin, charge density, energy band structure, and electronic state of carbon materials. Consequently, it can improve the electrocatalytic activity of carbon materials by introducing defects, holes, and more catalytically active sites [53,54]. The doping modification of  $C_{60}$  by heteroatoms (N, B, S, P, Si) has received extensive attention. Wang et al. [55] studied the influence of N, P, and Si doping on the catalytic activity of  $C_{60}$  in ORR by density functional theory (DFT). They found that heteroatom doping induces charge redistribution (Figure 4a). Besides, the catalysts' free energy curve has been proved to be an efficient method to estimate the ORR catalytic performance. It shows that  $C_{59}N$  and  $C_{59}Si$  were the best and worst ORR catalysts, respectively (Figure 4b). Meanwhile,  $C_{60}$  with the high curvature and pentagonal defect has a high ORR catalytic activity. Chen et al. [56] paid attention to the ORR mechanism and catalytic performance of pure fullerenes and N-doped fullerenes in combination with DFT. They investigated the size effect of pure doped fullerenes on the ORR activity. The results reveal that the smallest ( $C_{20}$  and  $C_{19}N$ ) and the largest ( $C_{180}$  and  $C_{179}N$ ) fullerenes enable strong adsorption of the ORR species. In contrast,  $C_{39}N$  with the reduced energy of the rate-determining step manifests a high ORR activity. Furthermore, the catalytic ORR pathway on  $C_{39}N$  was predicted:  $O_2 \rightarrow *O_2 \rightarrow *O + *OH \rightarrow *O + H_2O \rightarrow *OH + H_2O \rightarrow 2H_2O$  (Figure 4c,d). Seung Hyo Noh et al. [57] discussed the effect of nitrogen doping content on the OER and ORR catalytic activities of nitrogen-doped fullerenes. Combined with DFT

calculations, the experiment showed that nitrogen-doped fullerenes with a 10% doping content had a higher bifunctional catalytic activity (Figure 4e,f). In conclusion, strategies such as introducing defects and doping can be used to develop efficient fullerene-based metal-free electrocatalysts for electrochemical energy storage and conversion systems.

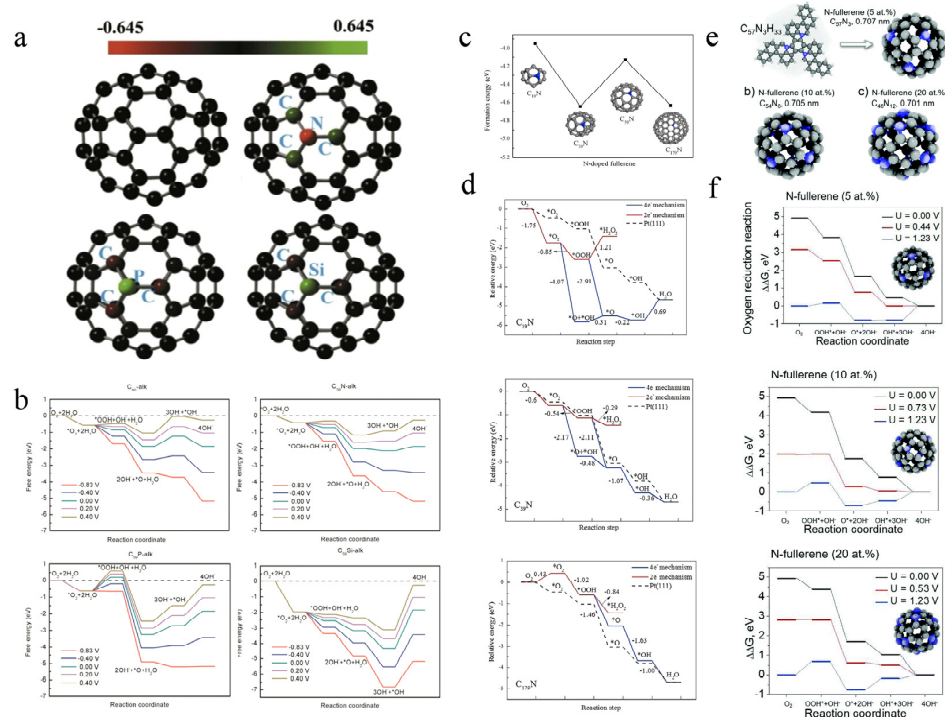


**Figure 4.** (a) Mulliken charge distribution on C<sub>60</sub>, C<sub>59</sub>N, C<sub>59</sub>P, C<sub>59</sub>Si. (b) Free-energy diagrams for the reduction of O<sub>2</sub> at different electrode potentials, U, in alkaline medium on C<sub>60</sub>, C<sub>59</sub>N, C<sub>59</sub>P, C<sub>59</sub>Si. Reproduced with permission [55]. Copyright 2017, Elsevier Ltd. (c) Calculated formation energies of N-doped fullerenes. (d) Relative energy profiles of the possible ORR pathways. Reproduced with permission [56]. Copyright 2017, Elsevier Ltd. (e) N-Fullerene of the 5 at% N aromatic precursor with C<sub>57</sub>N<sub>3</sub>H<sub>33</sub> molecules, and azafullerenes doped with N-doping levels of 10 and 20 at%, respectively. (f) Gibbs free energy diagrams of ORR in alkaline media with N-doping levels of 5, 10, and 20 at%. Used with permission [57]. Copyright 2017, The Royal Society of Chemistry.

## 4.2. Fullerene-Based Composites

### 4.2.1. Metals and Metal Oxides

A catalyst's support, which impacts the activity and durability of the catalyst [58], should have excellent electrical conductivity, corrosion resistance, and a large specific surface area, and ensure uniform and stable attachment of the active catalyst nanoparticles. C<sub>60</sub> has the characteristics of a particular shape, strong donor-acceptor charge transfer ability, and easy-to-regulate morphology, which provide the possibility for it to become an excellent catalyst carrier [59,60]. Considering these factors, Gopalan Saianand et al. [61] prepared Cu/Cu<sub>2</sub>O nanoparticles (NPs) anchored on mesoporous fullerenes (MFC<sub>60</sub>) by hard template synthesis method and wet impregnation (Figure 5a,b). The obtained Cu/Cu<sub>2</sub>O-MFC<sub>60</sub> catalysts with a 15 wt.% Cu/Cu<sub>2</sub>O NPs loading had the highest ORR catalytic activity among the investigated electrodes. It achieved an onset potential of 0.86 V vs. reversible hydrogen electrode (RHE) and a diffusion-limiting current density of  $-5.18 \text{ mA cm}^{-2}$  (Figure 5c,d). In detail, the excellent catalytic activity of Cu/Cu<sub>2</sub>O-MFC<sub>60</sub> was mainly attributed to the well-ordered mesoporous properties, abundant active sites, suitable specific surface area, and synergistic coupling effect of Cu/Cu<sub>2</sub>O NPs and C<sub>60</sub>. Mercy R. Benzigar et al. [62] adopted a hard template method to load highly crystalline  $\alpha$ -Fe<sub>2</sub>O<sub>3</sub> onto mesoporous C<sub>60</sub> to synthesize a Fe-MFC<sub>60</sub> catalyst (Figure 5e), which dis-

plays high ORR catalytic activity with an onset potential at 0.85 V vs. RHE and half-wave potential at 0.78 V vs. RHE (Figure 5f,g).

Studies have shown that metal encapsulation of carbon materials can also improve catalytic activity and stability [63,64]. Compared with other two-dimensional supported materials, the most significant difference of  $C_{60}$  is its larger hollow spherical structure, which allows encapsulating metal nanoparticles. He et al. [65] reported that  $M@C_{60}$  ( $M = Na, K, Rb, Cs, Sc, Ti, Mn, Fe$ ) had a high HER catalytic activity when  $C_{60}$  was separated into 20 metal atoms, which was mainly because the charge transfer of metal atoms to  $C_{60}$  changes the charge distribution and enhances the adsorption strength of H atoms on  $M@C_{60}$ . Chen et al. [66] focused on the catalytic performance of  $C_{60}$  encapsulated bimetals  $M_1xM_24-x@C_n$  ( $M_1xM_24-x$  represents  $Fe_xCo_{4-x}, Fe_xNi_{4-x}, Co_xNi_{4-x}$ ;  $x = 1, 2, 3$ ;  $n = 40, 50, 60$ ) by using DFT methods. Notably, the smaller fullerenes led to the greater charge transfer between the alloy core and the carbon shell, which was also confirmed by the most positive charges on the active site of  $Co_3Ni_1@C_{40}$  (Figure 5h). Furthermore, the volcano relationship indicated that  $Co_1Ni_3@C_{50}$  and  $Co_2Ni_2@C_{60}$  yielded high ORR activity ( $\eta^{ORR} = 0.35$  V) and OER activity ( $\eta^{OER} = 0.36$  V), respectively (Figure 5i,j).

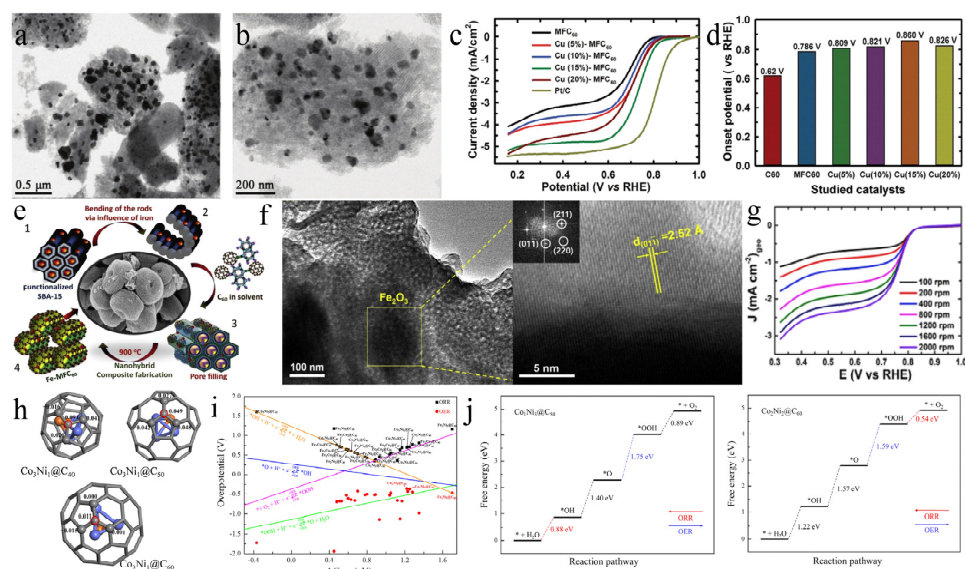


**Figure 5.** (a) Low and (b) high resolution TEM images of Cu(15%)-MFC<sub>60</sub>. (c) Consolidated ORR polarization curves were recorded at 1600 rpm in O<sub>2</sub>-saturated 0.1 M KOH (scan rate: 10 mV s<sup>-1</sup>) for the studied catalysts. (d) The respective onset potential. Reproduced with permission [61]. Copyright 2020, Elsevier Ltd. (e) Pictorial representation of mesoporous iron oxide C<sub>60</sub> (Fe-MFC<sub>60</sub>). (f) TEM images of Fe-MFC<sub>60</sub>-150. (g) Linear Sweep Voltammetry (LSV) curves of Fe-MFC<sub>60</sub>-150 were recorded in O<sub>2</sub>-saturated 0.5 M KOH at different rotation speeds. Reproduced with permission [62]. Copyright 2019, Elsevier Inc. (h) Charge distributions on Co<sub>3</sub>Ni<sub>1</sub>@C<sub>40</sub>, Co<sub>3</sub>Ni<sub>1</sub>@C<sub>50</sub>, and Co<sub>3</sub>Ni<sub>1</sub>@C<sub>60</sub>. (i) The volcano relationship between overpotential and  $\Delta G^*_{OH}$ . (j) Free energy diagrams of ORR and OER on Co<sub>1</sub>Ni<sub>3</sub>@C<sub>50</sub> and Co<sub>2</sub>Ni<sub>2</sub>@C<sub>60</sub>. Reproduced with permission [66]. Copyright 2021, Elsevier B.V.

#### 4.2.2. Molybdenum Disulfide

As the most representative transition metal dichalcogenide material, molybdenum disulfide (MoS<sub>2</sub>) is an excellent HER electrocatalyst due to its great planar active sites (active edges, S-vacancies, and grain boundaries) and high planar carrier mobility [67,68]. Yun-Hyuk Choi et al. [69] utilized a step-wise synthesis method including vapor transport, reduction, and topochemical sulfidation to grow 3D MoS<sub>2</sub> nanosheets on carbon fiber paper (CFP) substrates. Then, they used a simple solution deposition method to prepare 3D MoS<sub>2</sub> nanosheets and fullerene nanoclusters composite nC<sub>60</sub>/MoS<sub>2</sub>. The HER activity of nC<sub>60</sub>/MoS<sub>2</sub> was significantly enhanced due to the improved interfacial charge transfer of the hybrid nC<sub>60</sub>/MoS<sub>2</sub> p-n heterojunction. Based on the one-pot synthesis of vdW

MoS<sub>2</sub>/C<sub>60</sub> heterojunctions, Alain R. Puente Santiago et al. [70] studied the effect of C<sub>60</sub> concentration on the HER catalytic activity. The results showed a solid interfacial interaction between C<sub>60</sub> and MoS<sub>2</sub> in 1T-MoS<sub>2</sub>/C<sub>60</sub> supplemented with 20 wt% C<sub>60</sub>. The optimal binding strength of H atoms at the active site resulted in a Pt-like initial potential and an ultra-low  $\Delta G_{H^*}$  (−0.03 eV).

#### 4.2.3. Other Graphite Derivatives

C<sub>60</sub> has become a key component of functional micro/nanostructures due to its unique spherical structure, excellent electron-accepting ability, and high electron conductivity [36,71]. Aliyeh Hasanzadeh et al. [72] synthesized C<sub>60</sub>-CNTs hybrid materials by covalently connecting fullerenes with carbon nanotubes for efficient ORR. C<sub>60</sub>-CNTs possessed a large specific surface area, good intermolecular electronic transitions, fast mass transport, and defective sp<sup>3</sup>-C bonds, which promoted O<sub>2</sub> adsorption and OOH desorption. Gao et al. [73] reported a C<sub>60</sub> as the electron acceptor adsorbed on SWCNTs, which effectively induced charge transfer between C<sub>60</sub> and SWCNTs (Figure 6a). Raman spectra of C<sub>60</sub>-SWCNT<sub>n</sub> (*n* = 5, 10, and 15 min) exhibit an upshift in the peak position with increasing C<sub>60</sub> adsorption time (Figure 6b), which supports the charge transfer from SWCNTs to the electron-withdrawing C<sub>60</sub>. Moreover, the increased intensity ratio of the D-band to the G-band indicates that the nanotube structure became slightly more rich in defects (Figure 6b). The formed new metal-free, heteroatom/defect-free C<sub>60</sub>-SWCNTs material served as a multifunctional catalyst for ORR, OER, and HER over a wide pH range (Figure 6c–j).

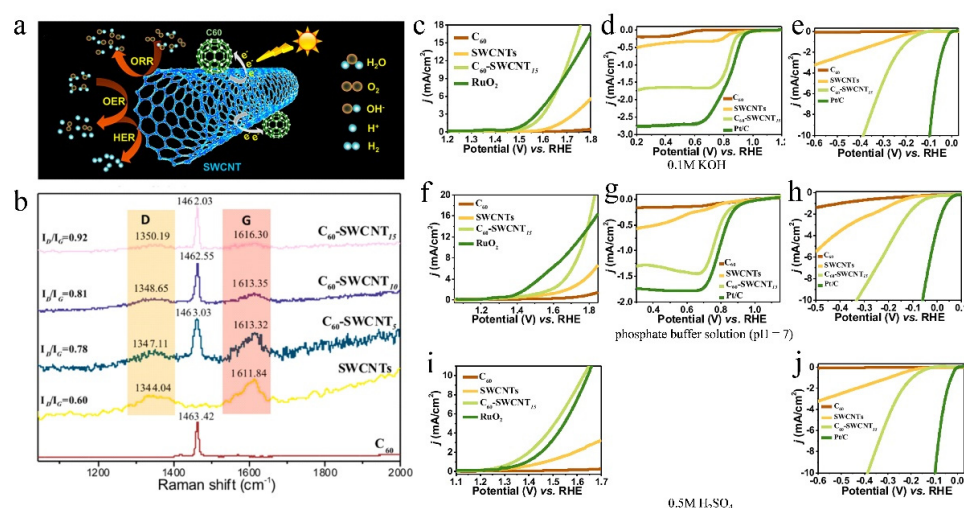


**Figure 6.** (a) Illustration of charge-transfer process and ORR/OER/HER on C<sub>60</sub>-SWCNTs. (b) Raman spectra of C<sub>60</sub> and C<sub>60</sub>-SWCNT<sub>n</sub> (*n* = 0, 5, 10, and 15 min). LSVs of (c) OER, (d) ORR, and (e) HER for pure C<sub>60</sub>, SWCNTs, C<sub>60</sub>-SWCNT<sub>15</sub>, and RuO<sub>2</sub> in 0.1 M KOH. LSVs of (f) OER, (g) ORR, and (h) HER for pure C<sub>60</sub>, SWCNTs, C<sub>60</sub>-SWCNT<sub>15</sub>, and RuO<sub>2</sub> in phosphate-buffered solution. LSVs of (i) OER, and (j) HER for pure C<sub>60</sub>, SWCNTs, C<sub>60</sub>-SWCNT<sub>15</sub>, and RuO<sub>2</sub> in 0.5 M H<sub>2</sub>SO<sub>4</sub>. Reproduced with permission [73]. Copyright 2019, American Chemical Society.

## 5. Application of Carbon Nanotubes in Electrocatalysis

### 5.1. Doping Effect

#### 5.1.1. Nitrogen Doping

Carbon nanotubes have been widely used in electrocatalysis due to their sufficient surface area, high conductivity, and well-established surface modification. However, the defects of CNTs, such as aggregation, chemical inertness, and solubility, are not insignificant. Existing methods, such as introducing defects, hetero-doping, and surface modification, have been used to modify CNTs. Notably, N-doping of carbon nanotubes (NCNTs) surfaces effectively controls the electronic structure and charge density distribution and generates more active sites, thus improving chemical reactivity [74]. Several locations accepting nitro-



gen doping in the carbon structure affect the catalytic activity of nitrogen-doped carbon materials. The common N doping types mainly include pyridinic N (398.6 eV), pyrrolic N (400.6 eV), and graphitic N (401.6 eV) (Figure 7a) [75]. Huang et al. [76] successfully developed NCNTs with fixed defect concentration by low-temperature preheating. They found that the higher the temperature for nitrogen doping, the higher the graphite N content. Moreover, combined with characterization, pyridinic N and pyrrolic N were identified as the active sites for the two-electron ORR pathway, while graphitic N accelerated the four-electron ORR pathway. The precise nitrogen doping can not only determine the real active sites of the catalyst but also explore the relationship between structure and properties. Ma et al. [77] synthesized NCNTs with a high concentration of pyridinic N (62.3% of the total nitrogen) by pyrolysis. The high concentration of pyridinic N, combined with gas-phase CO<sub>2</sub> electrolysis, was proved to effectively enhance the enrichment of CO<sub>2</sub> on the surface of NCNTs, which promoted the subsequent CO<sub>2</sub>RR reaction (Figure 7b). Furthermore, based on the DFT calculations of the CO<sub>2</sub> reduction reaction on NCNTs, the author demonstrated that electron transfer (red arrow in Figure 7c) becomes the rate-determining step (RDS), which attributes to high pyridinic N concentration.

Nitrogen-doped carbon nanotubes' wall number and growth mode also affect catalytic activity. Zhang et al. [78] found that NCNTs with an average wall number of 2.5 had higher ORR catalytic activity. For this sample, the inner layer provided an effective conductive path to transfer electrons from the inner layer to the outer layer through the tunneling effect. Nevertheless, the tunneling effect became weaker with increasing or decreasing the wall number of NCNTs, leading to the falling catalytic activity of NCNTs, which was further experimentally validated by others [79,80]. Besides, Yang et al. [81] focused on the active source of pure SWCNTs and non-metal-doped SWCNTs in the ORR process. They found that the pyramidalization angle is an excellent descriptor to study ORR activity on nitrogen- and boron-doped and undoped SWCNTs through machine learning tools, which enables prediction of the optimal diameter and the best doping type for the SWCNTs surfaces during the ORR. Li et al. [82] successfully prepared cactus-like NCNTs by directional growth using layered double hydroxides (LDHs) as catalyst precursors and metal-organic frameworks (MOFs) particles as carbon and nitrogen sources. Due to the unique hierarchical array structure, uniform N doping, and low charge transfer resistance, NCNTs yielded high catalytic activity in ORR and OER. Wu et al. [83] developed Co/Co<sub>2</sub>P@NCNTs catalysts with Co/Co<sub>2</sub>P heterojunction encapsulated in bamboo-like N-doped carbon nanotubes (Figure 7d,e). The Co/Co<sub>2</sub>P@NCNTs with the effect of abundant pyridinic N and graphitic N active sites, and highly ordered NCNTs, significantly enhanced the ORR kinetics and effectively attenuated the negative effects of high oxidation potential (during the OER process) on the ORR performance in alkaline electrolyte, showing high ORR activity with a half-wave potential ( $E_{1/2}$ ) of 0.87 V (Figure 7f). Meanwhile, the dynamic active state transformation from the Co/Co<sub>2</sub>P heterojunctions into Co<sup>3+</sup> Oh-containing CoO<sub>x</sub>(OH)<sub>y</sub> active species contributed to the markedly improved OER catalytic activity (Figure 7g,h).

### 5.1.2. Polyatomic Doping

Carbon nanotubes doped with two or more heteroatoms can also significantly improve the catalytic performance, owing to the existence of doped atoms and the effect of synergistic coupling on carbon nanotubes. Qu et al. [84] synthesized N,S co-doped carbon nanotubes (N,S-CNT) by the two-step "graft-and-pyrolyze" method. The N,S-CNT catalysts with uniform and high concentration of S doping (5.6 at%) displayed superb OER and HER bifunctional catalytic activities in alkaline electrolytes. Furthermore, secondary S-doping had a crucial role in forming electrocatalytically active sites and enhancing charge transfer. Liu et al. [85] demonstrated that Ru@Co/N-CNTs were highly functional for HER in acid and alkaline electrolytes by anchoring Ru nanoclusters on Co/N-doped carbon nanotubes. In detail, the as-prepared optimal catalyst showed a remarkable performance with low overpotentials of 48 and 92 mV at 10 mA cm<sup>-2</sup> in alkaline and acidic media, respectively. The excellent stability and hydrogen production efficiency of Ru@Co/N-CNTs were mainly

attributed to a large ECSA and high exposure of Ru active sites. Based on the successful synthesis of B, N co-doped graphene nanosheets (BCN), Hassina Tabassum et al. [86] used polyethylene glycol (PEG) with different molecular weights as guiding agents to roll BCN into BCN nanotubes with adjustable sizes and atomic bonds. The synthetic catalyst with a large specific surface area, abundant active sites, high concentration of pyridinic N, and numerous B-C, N-C bonds exhibited high ORR and HER bifunctional catalytic activity.

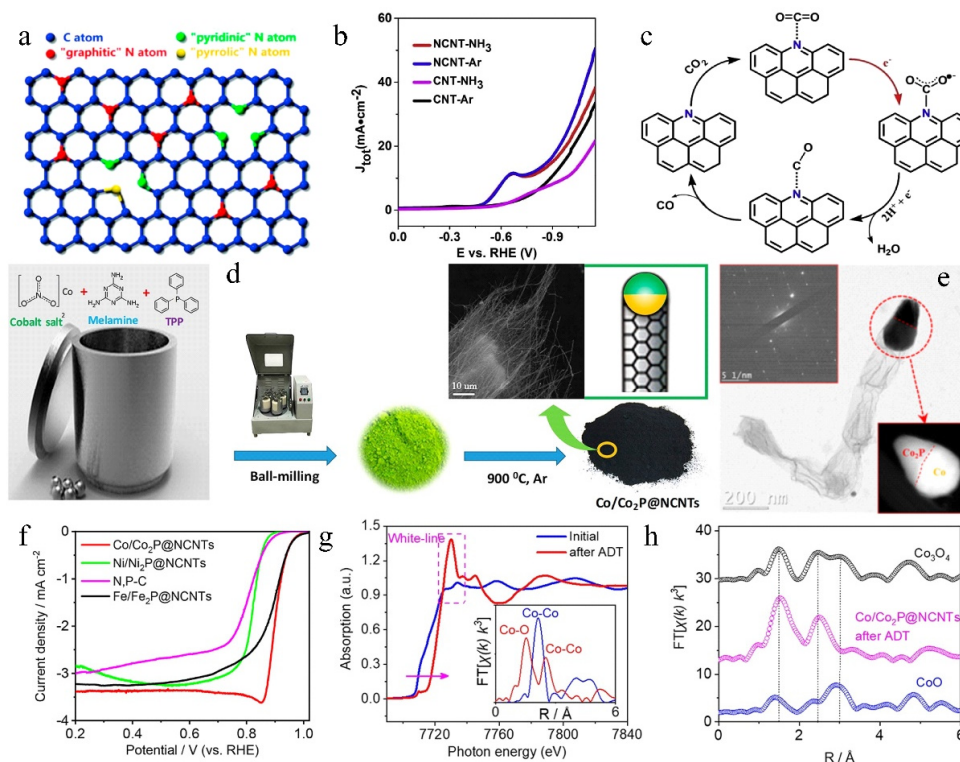


**Figure 7.** (a) Nitrogen doping into carbon plane at different locations. Reproduced with permission [75]. Copyright 2016, Elsevier Ltd. (b) LSV curves for NCNT-NH<sub>3</sub>, NCNT-Ar, CNT-NH<sub>3</sub>, and CNT-Ar in CO<sub>2</sub>-saturated 0.5 M NaHCO<sub>3</sub> aqueous solution at 50 mV s<sup>-1</sup>. (c) Mechanism of the CO<sub>2</sub> reduction reaction on NCNTs. Reproduced with permission [77]. Copyright 2019, American Chemical Society. (d) Schematic procedure for synthesizing the gram-scale Co/Co<sub>2</sub>P@NCNTs. (e) TEM images of the Co/Co<sub>2</sub>P@NCNTs. (f) ORR polarization plots of the M/M<sub>2</sub>P@NCNTs (M = Co, Ni, or Fe) and the N, P-C (rotation rate of 1600 rpm) in an O<sub>2</sub>-saturated 1.0 M KOH solution. (g) Normalized Co K-edge XANES spectra of the Co/Co<sub>2</sub>P@NCNTs before and after the accelerated cycling durability test, and (h) the corresponding magnitude Fourier transforms of Co K-edge EXAFS oscillations  $k^3\chi(k)$  ( $k$  weight of 3). The dashed vertical lines show the Co<sup>3+</sup>-O, Co<sup>3+</sup> Oh-Co<sup>3+</sup> Oh, and Co<sup>2+</sup> Td-Co<sup>3+</sup> Oh distances of 1.48, 2.44, and 3.03 Å, respectively. Reproduced with permission [83]. Copyright 2021, American Chemical Society.

## 5.2. Carrier Effect

Carbon nanotubes can be composited with monoatomic metals [87], metal oxides [88–90], and other graphite-derived carbon materials [91], to improve activity and durability [92]. As supported catalysts, it not only acts as a conductive carrier but also controls the electron distribution on the surface by utilizing the interaction with the supporting materials.

The beneficial effect of carbon nanotubes as a support has been demonstrated by strengthening the in-plane support and electrical conductivity of the composites. Li et al. [93] first synthesized pomegranate-like MoP@PC-CNTs by simple carbonization and phosphating process with POMOFs-CNTs composite as a precursor (Figure 8a,b). The introduction of CNTs offered more catalytic sites and enhanced long-range conductivity. Benefiting from the carrier, the composite displayed a low onset overpotential of 75 mV and a small Tafel slope of

55.9 mV dec<sup>-1</sup> for the HER (Figure 8c,d). Wu et al. [94] prepared an ORR and OER bifunctional electrocatalyst (Fe<sub>2</sub>Ni<sub>2</sub>N/Co@NCNT) with nanoclusters uniformly anchored on nitrogen-doped carbon nanotubes (Figure 8e,g). Due to the coupling effects in Fe<sub>2</sub>Ni<sub>2</sub>N/Co@NCNT, the electron transfer from the metal atoms (Fe, Ni) to the neighboring N and O atoms was revealed by the analysis of XAFS (Figure 8f). At the same time, the NCNT accelerated exchange kinetics of O<sup>2-</sup>/OH<sup>-</sup> and provided abundant contact area, strong adhesion, and low aggregation of Fe<sub>2</sub>Ni<sub>2</sub>N/Co nanoclusters. Hou et al. [95] prepared core-shell nanorods by coating ZnO with bimetallic zeolitic-imidazolate framework-NiZn (ZIF-NiZn), to obtain porous N-doped carbon nanotubes stabilized Ni SACs (Ni/NCTs) by a pyrolysis process. Based on EXAFS curves, the fitting result showed that the coordination number of Ni-N in Ni/NCTs-50 is near to that of NiPc with Ni-N<sub>4</sub> structure (Figure 8h). Due to the porous nanotube structure, high specific surface area, and atomized Ni-N coordination active sites, Ni/NCTs exhibited superior CO<sub>2</sub>RR activity with a CO Faradaic efficiency of nearly 100% over a wide potential range of -0.6 V to -1.0 V vs. RHE (Figure 8i-k).

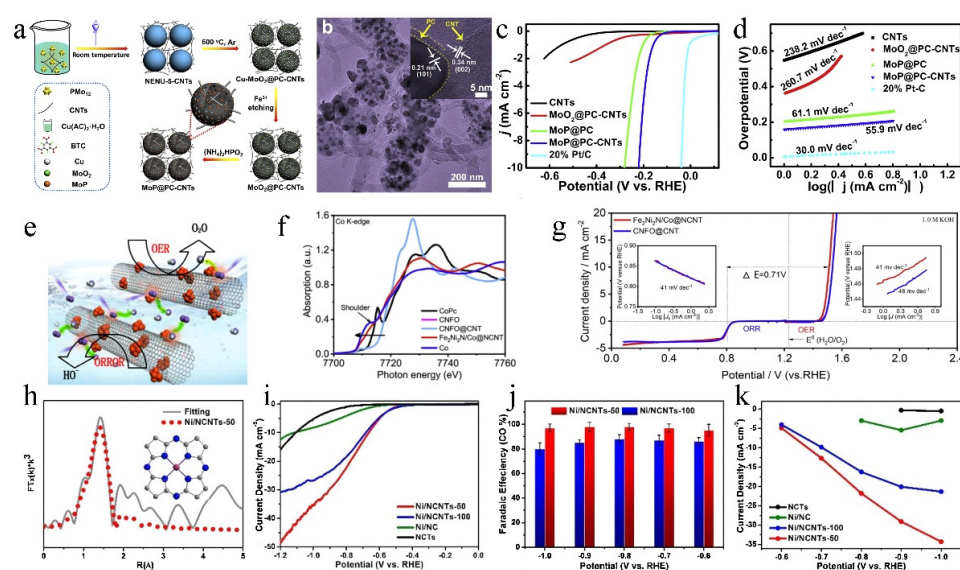


**Figure 8.** (a) Schematic illustration of the fabrication of MoP@PC-CNTs nanocomposite. (b) TEM images of MoP@PC-CNTs. (c) HER LSV curves of different catalysts and (d) the corresponding HER Tafel plots. Reproduced with permission [93]. Copyright 2018, Elsevier Ltd. (e) Illustration of ORR and OER on Fe<sub>2</sub>Ni<sub>2</sub>N/Co@NCNT. (f) Co K-edge XANES and spectra of various catalysts and standard samples, including FePc (Iron (II) phthalocyanine), CoPc (Cobalt (II) phthalocyanine) and NiPc (Nickel (II) phthalocyanine). (g) LSV curves for ORR and OER of Fe<sub>2</sub>Ni<sub>2</sub>N/Co@NCNT in O<sub>2</sub>-saturated 1.0 M KOH at a scan rate of 5 mV s<sup>-1</sup>, with the inset showing ORR (left) and OER (right) Tafel plots of the Fe<sub>2</sub>Ni<sub>2</sub>N/Co@NCNT. Reproduced with permission [94]. Copyright 2019, Elsevier Ltd. (h) The corresponding EXAFS fitting curves of Ni/NCTs-50. (i) LSV curves, (j) FE<sup>CO</sup> and (k) CO partial current densities for Ni/NCTs-50, Ni/NCTs-100, Ni/NC and NCTs in CO<sub>2</sub>-saturated 0.5 M KHCO<sub>3</sub> solution at various applied potentials. Reproduced with permission [95]. Copyright 2020, Elsevier B.V.

## 6. Application of Graphene in the Field of Electrocatalysis

### 6.1. Heteroatom Doping

Due to the advantages of extremely high surface area, high electron mobility, and variations of graphene doping structures, graphene has broad application prospects in various fields [96]. However, the inert carbon plane and zero band gap structure of impurity-free graphene, which exhibits poor electrocatalytic activity, are unsuitable for electrocatalysis [97]. Considering graphene's inert structure, heteroatom doping becomes an essential approach in graphene modification [98]. Graphene doping elements mainly include N, P, B, and S, which introduce defects, change the electronic structure near the

doped graphene atoms, and introduce more active sites, thus improving the catalytic activity [99–101].

#### 6.1.1. Single Atom Doping

N-doping has been the most intensively studied in the graphene doping electrocatalytic material. The role of N-doped graphene's active sites in ORR catalysis is still controversial. Yan et al. [102] performed simulation calculations on pure graphene, graphitic N, pyridine N, and graphene doped with graphitic N and pyridine N, respectively. The result indicated that the composite doping of graphitic nitrogen and pyridine nitrogen achieves charge redistribution, thereby promoting the adsorption of O<sub>2</sub>. Compared to mono-N-doping in graphene, binary-N-doped graphene possessed excellent catalytic activity for the CO<sub>2</sub>RR due to its stable adsorption of reactants [103]. Wang et al. [104] introduced several disordered structures through high-concentration KOH etching based on N-doped graphene. The experiments reveal that the high HER activity came from more active sites of dual defective graphene-based materials. In addition, many studies demonstrate that S- P-doping, B- P-doping, and P-doping also enhance the catalytic performance of graphene [105–108]. For instance, Li et al. [109] employed DFT to explore the ORR activity and mechanism of heteroatom-doped graphene catalysts with single X-doped graphene (X = N, P, As, Sb, S). They find that binding energies of \*OH (ORR intermediates) on the catalysts can serve as a descriptor for the ORR activity, which was attributed to the abundance of electronic states at the Fermi level.

#### 6.1.2. Polyatomic Doping

Compared with single heteroatom doping, polyatomic co-doped graphene is easier to introduce defects and modification of the electronic structure due to the synergistic effect between doping atoms, consequently leading to the enhancement of electrocatalytic activity [110–112]. Liang et al. [113] selected highly active N and S atoms as dopants to prepare N, S double-doped graphene (N-S-G). The ORR performance of N-S-G was significantly better than that of S single-doped (S-G) or N single-doped (N-G) catalysts. Additionally, DFT calculation confirmed that N, S double-doped graphene resulted in the redistribution of spin and charge density, leading to the enhancement of synergistic catalytic activity. Among double-doped graphene, the incorporation of metal elements enhances the electrical conductivity of doped graphene, thus exhibiting efficient catalytic performance [114–116]. Furthermore, Zhang et al. [117] prepared N, P, and F tri-doped graphene by a pyrolysis method. The corresponding synergistic effect of the doping atoms created highly active graphene-based ORR, OER, and HER catalysts.

### 6.2. Graphene Supported Metal

Because of the high electron transfer [6], advanced pore structure [118], great specific surface area [119], and easy coupling and synergistic effect with metals [120,121], graphene, especially doped graphene, has become a very popular candidate as a metal catalyst carrier.

#### 6.2.1. Single Atom Catalysts

Single-atom catalysts (SACs) have attracted extensive attention due to their sufficient atomic efficiency, high catalytic activity, and excellent selectivity among electrocatalytic materials. However, single-atom agglomeration without substrate has dramatically impeded the limited performance [122]. Doped graphene effectively alleviates atom agglomeration and provides a fantastic conductive substrate, enriches loading sites, and enhances single atom adsorption [123,124]. Zhang et al. [125] employed graphene oxide (GO) as a precursor to anchor atomic Fe-N<sub>4</sub> to nitrogen-doped graphene (Fe/NG) through simple heat treatment, yielding a catalyst with better CO<sub>2</sub>RR catalytic activity, high selectivity, and stability (Figure 9a–c). The isolated Fe-N<sub>4</sub> structure is more critical for the reduction of CO<sub>2</sub> to CO, which was confirmed by XAFS (Figure 9d,e). Furthermore, the mechanism of the CO<sub>2</sub> reduction reaction on Fe-N<sub>4</sub> moieties embedded in N-doped graphene showed a

potential promotional effect of nitrogen-doping of graphene (Figure 9f,g). Li et al. [126] also demonstrated that Fe-N<sub>4</sub> has impressive activity for CO<sub>2</sub>RR. Nitrogen-doped graphene-supported single Mo atoms (Mo@NG) [127] and single Ni atoms (Ni-NG) [128] have been confirmed to improve the CO<sub>2</sub>RR catalytic activity. However, the active sites of Mo@NG and Ni-NG were not the M-N<sub>4</sub> structure but the high dispersion of single metal atoms, abundant atomic catalytic efficiency, and the combined metal-N effect. Besides, N-doped graphene-supported single-atom Ni also exhibited unusual OER and ORR activities, which were attributed to the rich Ni doping, porous structure of N-doped graphene, and Ni, N co-doping (Figure 9h–k) [129].

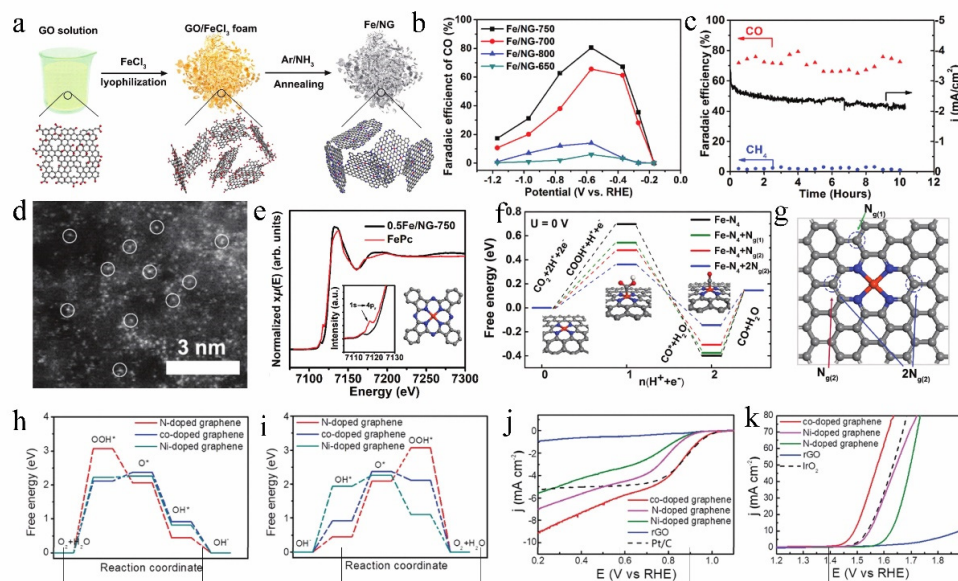


**Figure 9.** (a) Schematic of the synthesis process of the Fe/NG catalyst. (b) Potential dependence of CO FE for electrochemical CO<sub>2</sub> reduction on Fe/NG catalysts prepared at different annealing temperatures (in aqueous 0.1 M KHCO<sub>3</sub>). (c) Chronoamperometric curves of stability test with Fe/NG-750 at −0.60 V versus RHE in the CO<sub>2</sub>-saturated 0.1 M KHCO<sub>3</sub> solution. (d) HAADF-STEM images of Fe/NG–750 catalyst. (e) Normalized Fe K edge XANES spectra of 0.5Fe/NG-750 catalyst (black line) and FePc reference (red line); the inset shows the enlarged view of pre-edge features. (f) Free energy diagram for electrochemical CO<sub>2</sub> reduction to CO on FeN<sub>4</sub> moieties embedded on graphene sheets. (g) Top view of the optimized structures for Fe-N<sub>4</sub> moieties embedded on graphene layer and potential nitrogen-substitution. Reproduced with permission [125]. Copyright 2018, Wiley-VCH. Free energy diagrams for (h) the ORR and (i) OER processes. (j) ORR polarization curves of different electrodes in O<sub>2</sub>-saturated 0.1 M KOH. (k) OER polarization curves of different electrodes in 1.0 M KOH. Reproduced with permission [129]. Copyright 2019, Wiley-VCH.

## 6.2.2. Metals and Metal Oxides

Apart from highly dispersed metal single atoms, metal nanoparticles or metal nanoclusters also have particular activity owing to stable geometric structures, metal strain effect, and lattice defects [125,130–132]. Wang et al. [133] reported an electrocatalyst (Ir-NSG) with uniformly dispersed and intercalated Ir nanoclusters into N, S co-doped graphene. The superb performance in HER and OER originated from the Ir site's electronic state and coordination environment. N and S doping optimized the adsorption of hydrogen and oxygen intermediates on the Ir site and accelerated both HER and OER reaction kinetics. Meanwhile, N, S doped graphene provided a durable carrier and sufficient adsorption sites for Ir nanoclusters. Huang et al. [134] focused on the combination of metal nanoparticles and graphene, producing dispersed oxidized cobalt nanoparticles (5 nm) onto the monolayer of single-layer nitrogen-doped graphene (PO-5 nm Co/SL-NG) by a simple one-pot synthesis strategy. The synergistic effect of proton and electron multiple transfers in the CO<sub>2</sub>RR process is attributed to the high surface area, high conductivity, and synergy

with PO-5 nm Co of SL-NG. Besides the role of catalyst support, graphene can also act as a protective layer by coating metal nanoparticles [135]. For instance, a single-layer graphene covering the Cu surface effectively weakened the morphological changes of Cu during the electrocatalysis process and improved the catalytic stability [136]. In addition, metal oxides also yield good catalytic efficiency and selectivity due to the oxygen vacancy defects caused by oxygen introduction [137–140]. Particularly, Zhang et al. [141] deposited ultrasmall SnO<sub>2</sub> nanocrystals on the surface of nitrogen-doped graphene (SnO<sub>2</sub>/rGO) via an in situ conversion strategy, which resulted in an enhancement of the conversion efficiency and selectivity in the CO<sub>2</sub>RR. The oxygen vacancies in SnO<sub>2</sub> nanocrystals minimized severe agglomeration and poor electrical conductivity.

### 6.2.3. Other Metal Compounds

Benefits arising from the changes in the electronic structure and coordination environment caused by non-metallic elements, metal phosphides [142], metal nitrides [143], and metal sulfides [144] have tremendous implications for electrocatalysis applications [145,146]. Guo et al. [147] synthesized (N, S)-RGO@CoN by combining spray drying and atomic layer deposition, producing a catalyst that showed efficient and durable OER performance in the neutral electrolyte. The improved OER performance was related to the synergistic effects of short charge transfer paths, abundant active sites, and stable chemical coupling with CoN provided by the (N, S)-RGO substrate. At the same time, the unique 3D structure of P, S double-doped rGO(PSG) had also been confirmed to be beneficial for exposing more active sites and promoting the mass transfer of the electrolyte to electroactive sites on the electrocatalyst [148].

### 6.3. Graphene Quantum Dots

As the carbon material family's new member, graphene quantum dots (GQDs) are a 0D graphene material, which is characterized by 1 or 2 layers of graphitic planes with lateral dimensions typically <10 nm [149]. Compared with 2D graphene, the GQDs are currently explored as potential electrocatalysis due to unique advantages such as excellent dispersion, high surface area, facile chemical modification, abundant active sites, and surface functional groups [150–152]. When the size of the carrier is reduced to the GQDs level, the single atom on the catalyst surface is isolated from each other, which can impressively improve that single atomic load. For example, Xia et al. [153] used GQDs as intermediate carbon supports to increase the loading of Ni atoms, thereby improving the catalytic activity of the CO<sub>2</sub>RR reaction (Figure 10a,b). Simultaneously, Tran Van Tam et al. [154] focused on doped graphene quantum dots (BGQDs) with higher B doping content (4.25%), which improved CO<sub>2</sub>RR catalytic activity compared to GQDs. Compared with N single-doped GQDs, the N and S Co-doped GQDs changed the N doping state due to the introduction of S, resulting in the generation of asymmetric spin and the increase of charge density, thus showing improved activity [155]. In addition, heterojunctions have become an emerging frontier trend in electrocatalysis due to their synergistic effects, strain effects, and electronic interactions [156]. Gong et al. [157] reported a strategy to compound 2D microsheets with a large number of 0D/2D van der Waals heterojunctions (vdWHs) on the surface (Figure 10c,d). Using amphiphilic GQDs as intercalators and dispersants, the N and S Co-doped GQDs formed van der Waals heterojunctions with 2D graphene sheets. The GQD/MoS<sub>2</sub> van der Waals heterojunctions(GQD/MoS<sub>2</sub> vdWHs) significantly reduced HER overpotential and improved the electrode's long-term stability because of the synergistic coupling effect with the OD/2D heterojunction (Figure 10e,f) [158].

### 6.4. Other Graphene-Based Composites

Given the strong van der Waals interactions in the preparation process, graphene is prone to aggregation and stacking, which reduces active sites and mass transport rate during the catalytic process, which seriously affects its electrocatalytic activity [159–161]. To solve these issues, several feasible methods have been reported for designing 3D structure

nanocomposites composed of carbon nanotubes [162], 3D graphite foams [163,164], and graphene. Yang et al. [165] assembled carbon nanotubes and graphene into N, P co-doped hybrid nanosphere aerosols (N, P-CGHNs), which effectively prevented graphene stacking. The hybrid structure could form efficient charge transfer pathways that synergistically improved the ORR reaction electron transfer efficiency. Moreover, Mohammad Tavakkoli et al. [166] prepared N-Co-Mo-GF/CNT loaded simultaneously with single atoms of N, Co, and Mo by vapor deposition method using the graphene nanosheet (GF)-carbon nanotube (CNT) hybrid structure as the carrier. This GF/CNT, with high specific surface area and mesoporous structure, promoted mass transport during the catalytic reaction, thereby enhancing the catalytic activity of the ORR and OER reactions. However, in contrast to other hybrid designs of graphene and carbon nanotubes, Lai et al. [167] constructed N, S co-doped carbon nanotube/graphene nanosheet composites (N–S–CNTs) with a unique 3D structure, yielding high electrical conductivity, uniform dispersion of Ni<sub>3</sub>Fe, and exposure of active electrocatalytic sites.

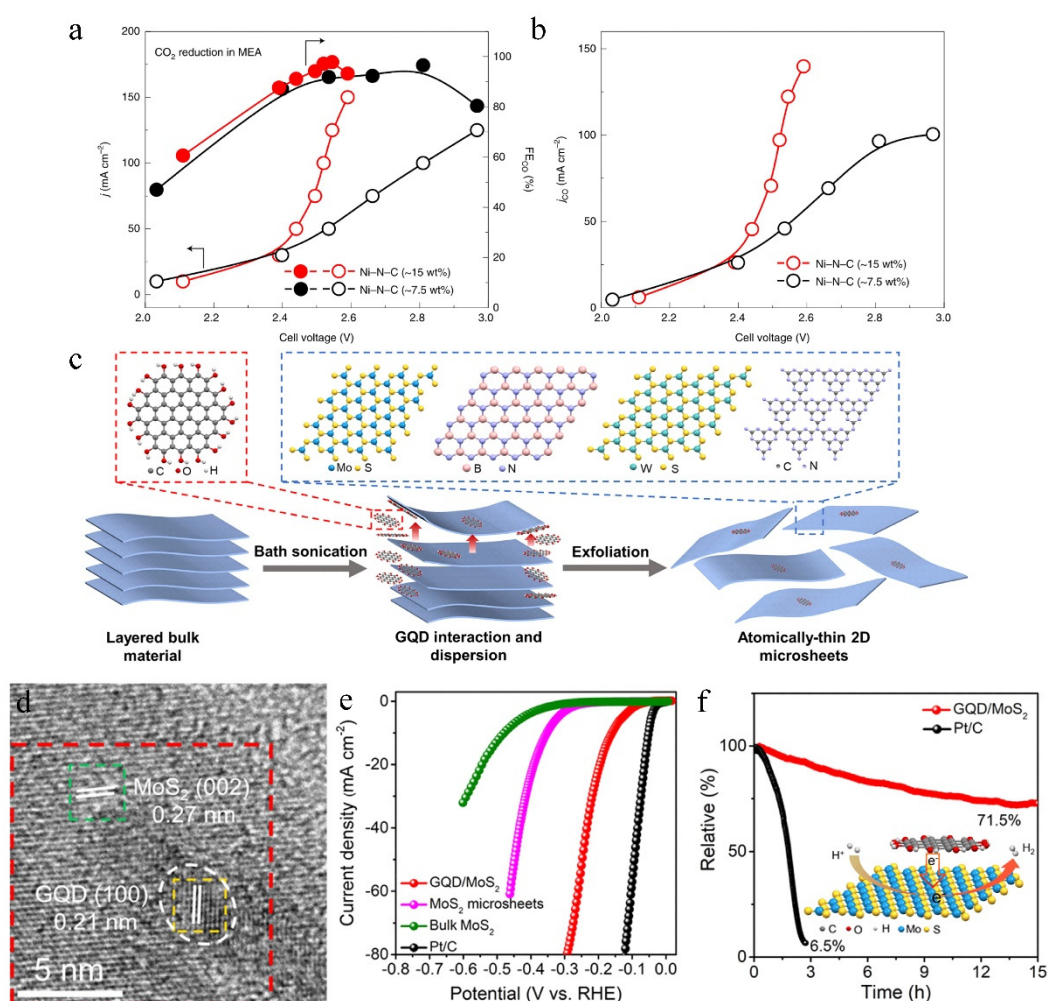


**Figure 10.** (a) The steady-state current densities and the corresponding Faradaic efficiencies of CO ( $FE_{CO}$ ) of ~7.5 wt% Ni-N-C and ~15 wt% Ni-N-C catalyst in an anion membrane electrode assembly (MEA). (b) The corresponding CO partial current densities ( $j_{CO}$ ) of ~7.5 wt% Ni-N-C and ~15 wt% Ni-N-C catalyst at different applied cell voltages. Reproduced with permission [153]. Copyright 2021, Nature Publishing Group. (c) Schematic illustration of GQD-assisted exfoliation of MoS<sub>2</sub>, h-BN, WS<sub>2</sub> and g-C<sub>3</sub>N<sub>4</sub> microsheets. (d) HRTEM images of GQD/MoS<sub>2</sub>. (e) Polarization curves of bulk MoS<sub>2</sub>. (f) Stability test of GQD/MoS<sub>2</sub> and Pt/C. Reproduced with permission [158]. Copyright 2021, Elsevier Ltd.

## 7. Conclusions and Perspective

The recent advances in the design of electrocatalysts for ORR, OER, HER, and CO<sub>2</sub>RR based on graphite-derived materials have been summarized in this manuscript, and the performance-related information is presented in Table 1. There are generally two strategies to improve the electrocatalytic activity: (i) increasing the intrinsic activity of catalysts, and (ii) increasing the number of exposed active sites. This paper discusses structural regulation strategies and carrier function of graphite-derived materials for the above-mentioned electrochemical reactions in terms of: (1) hetero doping modification, (2) defect control, (3) heterojunction introduction, and (4) uniformity of metal active electrocatalyst dispersion.

**Table 1.** Summary of Catalytic performance of discussed catalysts in the main text.

Catalysts	Strategies	Catalytic Performance/ vs. RHE	Ref.
Cu/Cu <sub>2</sub> O-MFC <sub>60</sub>	Loaded Defect	ORR 0.86 V@E <sub>onset</sub> , −5.183 mA cm <sup>−2</sup> @diffusion-limiting current density	[61]
Fe-MFC <sub>60</sub>	Doped Loaded	ORR 0.85 V@E <sub>onset</sub> , 0.78 V@E <sub>1/2</sub>	[62]
ANG	co-doped	ORR 0.99 V@E <sub>onset</sub> , 0.85 V@E <sub>1/2</sub> , 4.5 mA cm <sup>−2</sup> Current density at 0.8 V	[114]
CPS@G <sub>N,S,P</sub>	Doped Loaded	ORR 0.8 V@E <sub>1/2</sub> , 29 mV dec <sup>−1</sup> @ Tafel slope	[142]
N,P-CGHNs	Doped Loaded	ORR 0.94 V@E <sub>onset</sub> , 0.82 V@E <sub>1/2</sub>	[165]
10% F/BCN	Doped Loaded	ORR 0.92 V@E <sub>onset</sub> , 0.79 V@E <sub>1/2</sub> , 12 h at 0.75 V@ Stability OER 390 mV@η <sub>10</sub> , 79 mV dec <sup>−1</sup> @ Tafel slope HER 0.042 V@E <sub>onset</sub> , 87 mV dec <sup>−1</sup> @ Tafel slope	[71]
Co/Co <sub>2</sub> P@NCNTs	Doped Loaded	ORR 0.90 V@E <sub>1/2</sub> OER 480 mV@η <sub>50</sub> , 1.58 V@E <sub>j=10</sub> ORR 96% current retention after a long-term 50 h test	[83]
np-graphene	co-doped Defect	ORR 1.45 V@E <sub>onset</sub> , 270 mV@η <sub>10</sub> , 59 mV dec <sup>−1</sup> @ Tafel slope ORR 0.878 V@E <sub>1/2</sub> , 40 mV dec <sup>−1</sup> @ Tafel slope	[129]
S-Ni <sub>3</sub> FeN/NSG	co-doped	OER 260 mV@η <sub>10</sub> , 76 mV dec <sup>−1</sup> @ Tafel slope	[143]
Ni <sub>3</sub> Fe/N-S-CNTs	co-doped Loaded	ORR 0.877 V@E <sub>1/2</sub> , 353 mV@η <sub>10</sub> , 43.2 mV dec <sup>−1</sup> @ Tafel slope OER 215 mV@η <sub>10</sub> , 44.1 mV dec <sup>−1</sup> @ Tafel slope OER 1.59 V@E <sub>j=10</sub> ,	[167]
N,S-CNT	co-doped	56 mV dec <sup>−1</sup> @ Tafel slope HER −0.4 V at 5 mA cm <sup>−2</sup> , 133 mV dec <sup>−1</sup> @ Tafel slope OER 280 mV@η <sub>10</sub> ,	[84]
Co <sub>2</sub> P@N,P-PCN/CNTs	co-doped Loaded	72 mV dec <sup>−1</sup> @ Tafel slope HER 154 mV@η <sub>10</sub> , 52 mV dec <sup>−1</sup> @ Tafel slope OER 307 mV@η <sub>10</sub> ,	[88]
Ir-NSG	co-doped Loaded	74.2 mV dec <sup>−1</sup> @ Tafel slope HER 22 mV@η <sub>10</sub> , 21.2 mV dec <sup>−1</sup> @ Tafel slope HER in 1 M KOH 48 mV@η <sub>10</sub> , 33 mV dec <sup>−1</sup> @ Tafel slope, 0.25 s <sup>−1</sup> at −0.05 V @ TOF	[133]
Ru@Co/N-CNTs	co-doped Loaded	HER in 0.5 M H <sub>2</sub> SO <sub>4</sub> 92 mV@η <sub>10</sub> , 45 mV dec <sup>−1</sup> @ Tafel slope	[85]
R-PtO <sub>x</sub> /CNT	Doped Loaded	HER 19.4 mV@η <sub>10</sub> , 34.6 mV dec <sup>−1</sup> @ Tafel slope	[89]



Table 1. Cont.

Catalysts	Strategies	Catalytic Performance/vs. RHE	Ref.
Ni/NiS/P,N,S-rGO	co-doped Defect van der	HER 155 mV@ $\eta$ 10, 135 mV dec <sup>-1</sup> @ Tafel slope	[144]
GQD/MoS <sub>2</sub>	Waals hetero- junction	HER 160 mV@ $\eta$ 10, 56.9 mV dec <sup>-1</sup> @ Tafel slope	[158]
NCNTs	Rich-doped	CO <sub>2</sub> RR > 94.5%@FE, 20.2 mA cm <sup>-2</sup> at -(0.6–0.9 V)	[77]
Ni/NCTs-50	Doped Loaded	CO <sub>2</sub> RR 9366 h <sup>-1</sup> @TOF, 98%@FE, 34.3 mA cm <sup>-2</sup> at -1.0 V	[95]
Fe/NG-750	Doped Loaded	CO <sub>2</sub> RR $\approx$ 80%@FE	[125]
PO-5 nm -Co/SL-NG	Doped Loaded	CO <sub>2</sub> RR(versus SCE) 380 mV $\eta$ 10, 71.4%@FE at -0.90 V	[134]
SnO <sub>2</sub> @N-rGO	Doped Loaded	CO <sub>2</sub> RR 21.3 mA cm <sup>-2</sup> at -0.8 V, 89%@FE	[141]
15 wt% Ni-N-C	GQD loaded high single-atom	CO <sub>2</sub> RR 122 mA cm <sup>-2</sup> @CO partial current	[153]

Based on the review of the literature presented in the current manuscript, the following are the recommendations proposed:

- (1) Deeper insights into the electrocatalytic active sites of modified graphite-derives are required, especially doped graphite-derived materials. Advanced operando characterization methods are also necessary to deeply explore the effect of doping on the electronic distribution of active sites. By combining theoretical DFT simulations and various advanced in situ characterization methods, including in situ X-ray diffraction (XRD), X-ray absorption spectra (XAS), Raman, and Fourier-transform infrared (FTIR), the role of doping can be well understood.
- (2) Systematic understanding of the carrier role of graphite-derived materials. Due to the large specific surface area, easily regulated structures, and abundant active sites, the fullerenes, carbon nanotubes, and graphene can act as active catalysts and catalyst support for other active materials. Furthermore, the interfacial behavior between the carrier and the active catalyst should be paid more attention.
- (3) Catalyst activity measurement standards should be established to facilitate the comparison of the activity of electrocatalysts. Although researchers have developed many electrocatalysts over a few decades, it is still challenging to compare their performances due to the nonstandardized measurements (see Table 1). Therefore, the reports must establish a standard to appropriately and accurately compare electrocatalysts for ORR, OER, HER, and CO<sub>2</sub>RR.

**Author Contributions:** Conceptualization and writing—original draft preparation, S.H., M.W. and G.Z.; writing—review and editing, S.H., M.W., S.L., Z.J., H.H., S.G.C., H.Y., S.O., S.S. and G.Z. Project administration and funding acquisition—G.Z. and S.O. All authors have read and agreed to the published version of the manuscript.

**Funding:** This research was funded by the Natural Sciences and Engineering Research Council of Canada (NSERC), the National Natural Science Foundation of China (22208331), the Fonds de Recherche du Québec-Nature et Technologies (FRQNT), Centre Québécois sur les Matériaux Fonctionnels (CQMF), McGill University, École de Technologie Supérieure (ÉTS), Institut National de la Recherche Scientifique (INRS). Dr. G. Zhang thanks for the support from the Marcelle-Gauvreau Engineering Research Chair program.

**Institutional Review Board Statement:** Not applicable.

**Informed Consent Statement:** Not applicable.

**Data Availability Statement:** Not applicable.

**Conflicts of Interest:** The authors declare no conflict of interest.

## References

1. Craig, M.J.; Garcia-Melchor, M. Applying Active Learning to the Screening of Molecular Oxygen Evolution Catalysts. *Molecules* **2021**, *26*, 6362. [[CrossRef](#)] [[PubMed](#)]
2. Pu, J.; Zhang, K.; Wang, Z.; Li, C.; Zhu, K.; Yao, Y.; Hong, G. Synthesis and Modification of Boron Nitride Nanomaterials for Electrochemical Energy Storage: From Theory to Application. *Adv. Funct. Mater.* **2021**, *31*, 2106315. [[CrossRef](#)]
3. Park, J.; Kwon, T.; Kim, J.; Jin, H.; Kim, H.Y.; Kim, B.; Joo, S.H.; Lee, K. Hollow nanoparticles as emerging electrocatalysts for renewable energy conversion reactions. *Chem. Soc. Rev.* **2018**, *47*, 8173–8202. [[CrossRef](#)]
4. Wang, Y.; Cui, X.; Peng, L.; Li, L.; Qiao, J.; Huang, H.; Shi, J. Metal-Nitrogen-Carbon Catalysts of Specifically Coordinated Configurations toward Typical Electrochemical Redox Reactions. *Adv. Mater.* **2021**, *33*, 2100997. [[CrossRef](#)]
5. Wu, T.; Sun, M.-Z.; Huang, B.-L. Non-noble metal-based bifunctional electrocatalysts for hydrogen production. *Rare Met.* **2022**, *41*, 2169–2183. [[CrossRef](#)]
6. Zhao, S.; Wang, D.; Amal, R.; Dai, L. Carbon-Based Metal-Free Catalysts for Key Reactions Involved in Energy Conversion and Storage. *Adv. Mater.* **2019**, *31*, 1801526. [[CrossRef](#)] [[PubMed](#)]
7. Wang, J.; Kim, J.; Choi, S.; Wang, H.; Lim, J. A Review of Carbon-Supported Nonprecious Metals as Energy-Related Electrocatalysts. *Small Methods* **2020**, *4*, 2000621. [[CrossRef](#)]
8. Wang, J.; Kong, H.; Zhang, J.; Hao, Y.; Shao, Z.; Ciucci, F. Carbon-based electrocatalysts for sustainable energy applications. *Prog. Mater. Sci.* **2021**, *116*, 100717.
9. Xu, X.; Wang, S.; Guo, S.; San Hui, K.; Ma, J.; Dinh, D.A.; Hui, K.N.; Wang, H.; Zhang, L.; Zhou, G. Cobalt phosphosulfide nanoparticles encapsulated into heteroatom-doped carbon as bifunctional electrocatalyst for Zn–air battery. *Adv. Powder Mater.* **2022**, *1*, 100027. [[CrossRef](#)]
10. Sun, H.; Zhu, Y.; Jung, W. Tuning Reconstruction Level of Precatalysts to Design Advanced Oxygen Evolution Electrocatalysts. *Molecules* **2021**, *26*, 5476. [[CrossRef](#)]
11. Wang, H.-F.; Tang, C.; Zhang, Q. A Review of Precious-Metal-Free Bifunctional Oxygen Electrocatalysts: Rational Design and Applications in Zn–Air Batteries. *Adv. Funct. Mater.* **2018**, *28*, 1803329. [[CrossRef](#)]
12. Wu, M.; Zhang, G.; Du, L.; Yang, D.; Yang, H.; Sun, S. Defect Electrocatalysts and Alkaline Electrolyte Membranes in Solid-State Zinc-Air Batteries: Recent Advances, Challenges, and Future Perspectives. *Small Methods* **2021**, *5*, 2000868. [[CrossRef](#)]
13. Kuai, C.; Xu, Z.; Xi, C.; Hu, A.; Yang, Z.; Zhang, Y.; Sun, C.-J.; Li, L.; Sokaras, D.; Dong, C.; et al. Phase segregation reversibility in mixed-metal hydroxide water oxidation catalysts. *Nat. Catal.* **2020**, *3*, 743–753. [[CrossRef](#)]
14. Wang, J.; Xu, F.; Jin, H.; Chen, Y.; Wang, Y. Non-Noble Metal-based Carbon Composites in Hydrogen Evolution Reaction: Fundamentals to Applications. *Adv. Mater.* **2017**, *29*, 1605838. [[CrossRef](#)]
15. Wang, X.; Zheng, Y.; Sheng, W.; Xu, Z.; Jaroniec, M.; Qiao, S.-Z. Strategies for design of electrocatalysts for hydrogen evolution under alkaline conditions. *Mater. Today* **2020**, *36*, 125–138. [[CrossRef](#)]
16. Selvam, N.C.S.; Du, L.; Xia, B.; Yoo, P.J.; You, B. Reconstructed Water Oxidation Electrocatalysts: The Impact of Surface Dynamics on Intrinsic Activities. *Adv. Funct. Mater.* **2020**, *31*, 2008190. [[CrossRef](#)]
17. Seh, Z.W.; Kibsgaard, J.; Dickens, C.F.; Chorkendorff, I.; Norskov, J.K.; Jaramillo, T.F. Combining theory and experiment in electrocatalysis: Insights into materials design. *Science* **2017**, *355*, eaad4998. [[CrossRef](#)]
18. Peugeot, A.; Creissen, C.E.; Karapinar, D.; Tran, H.N.; Schreiber, M.; Fontecave, M. Benchmarking of oxygen evolution catalysts on porous nickel supports. *Joule* **2021**, *5*, 1281–1300. [[CrossRef](#)]
19. Charles, V.; Anumah, A.O.; Adegoke, K.A.; Adesina, M.O.; Ebuka, I.P.; Gaya, N.A.; Ogwuche, S.; Yakubu, M.O. Progress and challenges pertaining to the earthy-abundant electrocatalytic materials for oxygen evolution reaction. *Sustain. Mater. Technol.* **2021**, *28*, e00252. [[CrossRef](#)]
20. Lu, X.; Xia, B.; Zang, S.; Lou, X. Metal-Organic Frameworks Based Electrocatalysts for the Oxygen Reduction Reaction. *Angew. Chem. Int. Ed.* **2020**, *59*, 4634–4650. [[CrossRef](#)]
21. Zhang, L.; Zhang, J. Novel electrochemical half-cell design and fabrication for performance analysis of metal-air battery air-cathodes. *Int. J. Green Energy* **2018**, *16*, 236–241. [[CrossRef](#)]
22. Martinez, U.; Komini Babu, S.; Holby, E.F.; Chung, H.T.; Yin, X.; Zelenay, P. Progress in the Development of Fe-Based PGM-Free Electrocatalysts for the Oxygen Reduction Reaction. *Adv. Mater.* **2019**, *31*, 1806545. [[CrossRef](#)]
23. Bates, J.S.; Biswas, S.; Suh, S.E.; Johnson, M.R.; Mondal, B.; Root, T.W.; Stahl, S.S. Chemical and Electrochemical O<sub>2</sub> Reduction on Earth-Abundant M-N-C Catalysts and Implications for Mediated Electrolysis. *J. Am. Chem. Soc.* **2022**, *144*, 922–927. [[CrossRef](#)]
24. Birdja, Y.Y.; Pérez-Gallent, E.; Figueiredo, M.C.; Göttle, A.J.; Calle-Vallejo, F.; Koper, M.T.M. Advances and challenges in understanding the electrocatalytic conversion of carbon dioxide to fuels. *Nat. Energy* **2019**, *4*, 732–745. [[CrossRef](#)]
25. Bagger, A.; Ju, W.; Varela, A.S.; Strasser, P.; Rossmeisl, J. Electrochemical CO<sub>2</sub> Reduction: A Classification Problem. *Chemphyschem* **2017**, *18*, 3266–3273. [[CrossRef](#)]
26. Zheng, Y.; Vasileff, A.; Zhou, X.; Jiao, Y.; Jaroniec, M.; Qiao, S. Understanding the Roadmap for Electrochemical Reduction of CO<sub>2</sub> to Multi-Carbon Oxygenates and Hydrocarbons on Copper-Based Catalysts. *J. Am. Chem. Soc.* **2019**, *141*, 7646–7659. [[CrossRef](#)]
27. Yang, D.; Zhu, Q.; Han, B. Electroreduction of CO<sub>2</sub> in Ionic Liquid-Based Electrolytes. *Innovation* **2020**, *1*, 100016. [[CrossRef](#)]
28. Ross, M.B.; De Luna, P.; Li, Y.; Dinh, C.-T.; Kim, D.; Yang, P.; Sargent, E.H. Designing materials for electrochemical carbon dioxide recycling. *Nat. Catal.* **2019**, *2*, 648–658. [[CrossRef](#)]

29. Woldu, A.R.; Huang, Z.; Zhao, P.; Hu, L.; Astruc, D. Electrochemical CO<sub>2</sub> reduction (CO<sub>2</sub>RR) to multi-carbon products over copper-based catalysts. *Coord. Chem. Rev.* **2022**, *454*, 214340. [[CrossRef](#)]
30. Chia, X.; Pumera, M. Characteristics and performance of two-dimensional materials for electrocatalysis. *Nat. Catal.* **2018**, *1*, 909–921. [[CrossRef](#)]
31. Jara, A.D.; Betemariam, A.; Woldetinsae, G.; Kim, J.Y. Purification, application and current market trend of natural graphite: A review. *Int. J. Min. Sci. Technol.* **2019**, *29*, 671–689. [[CrossRef](#)]
32. Zhang, Z.; Yu, L.; Tu, Y.; Chen, R.; Wu, L.; Zhu, J.; Deng, D. Unveiling the Active Site of Metal-Free Nitrogen-doped Carbon for Electrocatalytic Carbon Dioxide Reduction. *Cell Rep. Phys. Sci.* **2020**, *1*, 100145. [[CrossRef](#)]
33. Feng, L.; Qin, Z.; Huang, Y.; Peng, K.; Wang, F.; Yan, Y.; Chen, Y. Boron-, sulfur-, and phosphorus-doped graphene for environmental applications. *Sci. Total Environ.* **2020**, *698*, 134239. [[CrossRef](#)]
34. Rodríguez-Pérez, I.A.; Zhang, L.; Wrogemann, J.M.; Driscoll, D.M.; Sushko, M.L.; Han, K.S.; Fulton, J.L.; Engelhard, M.H.; Balasubramanian, M.; Viswanathan, V.V.; et al. Enabling Natural Graphite in High-Voltage Aqueous Graphite || Zn Metal Dual-Ion Batteries. *Adv. Energy Mater.* **2020**, *10*, 2001256. [[CrossRef](#)]
35. Lin, X.; Zhang, X.; Liu, L.; Liang, J.; Liu, W. Polymer/expanded graphite-based flexible phase change material with high thermal conductivity for battery thermal management. *J. Clean. Prod.* **2022**, *331*, 130014. [[CrossRef](#)]
36. Xu, T.; Shen, W.; Huang, W.; Lu, X. Fullerene micro/nanostructures: Controlled synthesis and energy applications. *Mater. Today Nano* **2020**, *11*, 100081. [[CrossRef](#)]
37. Puente Santiago, A.R.; Fernandez-Delgado, O.; Gomez, A.; Ahsan, M.A.; Echegoyen, L. Fullerenes as Key Components for Low-Dimensional (Photo)electrocatalytic Nanohybrid Materials. *Angew. Chem. Int. Ed.* **2021**, *60*, 122–141. [[CrossRef](#)]
38. Jiang, Z.; Zhao, Y.; Lu, X.; Xie, J. Fullerenes for rechargeable battery applications: Recent developments and future perspectives. *J. Energy Chem.* **2021**, *55*, 70–79. [[CrossRef](#)]
39. Zhang, R.; Zhang, Y.; Wei, F. Horizontally aligned carbon nanotube arrays: Growth mechanism, controlled synthesis, characterization, properties and applications. *Chem. Soc. Rev.* **2017**, *46*, 3661–3715. [[CrossRef](#)]
40. He, M.; Zhang, S.; Zhang, J. Horizontal Single-Walled Carbon Nanotube Arrays: Controlled Synthesis, Characterizations, and Applications. *Chem. Rev.* **2020**, *120*, 12592–12684. [[CrossRef](#)]
41. Wu, Y.; Zhao, X.; Shang, Y.; Chang, S.; Dai, L.; Cao, A. Application-Driven Carbon Nanotube Functional Materials. *ACS Nano* **2021**, *15*, 7946–7974. [[CrossRef](#)]
42. Zhang, S.; Zhang, N.; Zhang, J. Controlled Synthesis of Carbon Nanotubes: Past, Present and Future. *Acta Phys. Chim. Sin.* **2020**, *36*, 1907021. [[CrossRef](#)]
43. Michael, F.L.; Sameh, H.T.; Ray, H.B.; John, H.A. Carbon Nanotubes: Present and Future Commercial Applications. *Science* **2013**, *339*, 535–539.
44. Zhu, Z.; Cui, C.; Bai, Y.; Gao, J.; Jiang, Y.; Li, B.; Wang, Y.; Zhang, Q.; Qian, W.; Wei, F. Advances in Precise Structure Control and Assembly toward the Carbon Nanotube Industry. *Adv. Funct. Mater.* **2021**, *32*, 2109401. [[CrossRef](#)]
45. Zhang, S.; Nguyen, N.; Leonhardt, B.; Jolowsky, C.; Hao, A.; Park, J.G.; Liang, R. Carbon-Nanotube-Based Electrical Conductors: Fabrication, Optimization, and Applications. *Adv. Electron. Mater.* **2019**, *5*, 1800811. [[CrossRef](#)]
46. Novoselov, K.S.; Geim, A.K.; Morozov, S.V.; Jiang, D.; Zhang, Y.; Dubonos, S.V.; Grigorieva, I.V.; Firsov, A.A. Electric field effect in atomically thin carbon films. *Science* **2004**, *306*, 666–669. [[CrossRef](#)]
47. Zhang, Y.-L.; Li, J.-C.; Zhou, H.; Liu, Y.-Q.; Han, D.-D.; Sun, H.-B. Electro-responsive actuators based on graphene. *Innovation* **2021**, *2*, 100168. [[CrossRef](#)]
48. Zhang, Y.; Wan, Q.; Yang, N. Recent Advances of Porous Graphene: Synthesis, Functionalization, and Electrochemical Applications. *Small* **2019**, *15*, e1903780. [[CrossRef](#)] [[PubMed](#)]
49. Qiu, B.; Xing, M.; Zhang, J. Recent advances in three-dimensional graphene based materials for catalysis applications. *Chem. Soc. Rev.* **2018**, *47*, 2165–2216. [[CrossRef](#)] [[PubMed](#)]
50. Novoselov, K.S.; Fal'ko, V.I.; Colombo, L.; Gellert, P.R.; Schwab, M.G.; Kim, K. A roadmap for graphene. *Nature* **2012**, *490*, 192–200. [[CrossRef](#)]
51. Joshi, D.J.; Koduru, J.R.; Malek, N.I.; Hussain, C.M.; Kailasa, S.K. Surface modifications and analytical applications of graphene oxide: A review. *TrAC Trends Anal. Chem.* **2021**, *144*, 116448. [[CrossRef](#)]
52. Geim, A.K.; Novoselov, K.S. The rise of graphene. *Nat. Mater.* **2007**, *6*, 183–191. [[CrossRef](#)] [[PubMed](#)]
53. Lin, Y.; Zhu, Y.; Zhang, B.; Kim, Y.A.; Endo, M.; Su, D.S. Boron-doped onion-like carbon with enriched substitutional boron: The relationship between electronic properties and catalytic performance. *J. Mater. Chem. A* **2015**, *3*, 21805–21814. [[CrossRef](#)]
54. María Girón, R.; Marco-Martínez, J.; Bellani, S.; Insuasty, A.; Comas Rojas, H.; Tullii, G.; Antognazza, M.R.; Filippone, S.; Martín, N. Synthesis of modified fullerenes for oxygen reduction reactions. *J. Mater. Chem. A* **2016**, *4*, 14284–14290. [[CrossRef](#)]
55. Wang, Y.; Jiao, M.; Song, W.; Wu, Z. Doped fullerene as a metal-free electrocatalyst for oxygen reduction reaction: A first-principles study. *Carbon* **2017**, *114*, 393–401. [[CrossRef](#)]
56. Chen, X.; Chang, J.; Ke, Q. Probing the activity of pure and N-doped fullerenes towards oxygen reduction reaction by density functional theory. *Carbon* **2018**, *126*, 53–57. [[CrossRef](#)]
57. Noh, S.H.; Kwon, C.; Hwang, J.; Ohsaka, T.; Kim, B.J.; Kim, T.Y.; Yoon, Y.G.; Chen, Z.; Seo, M.H.; Han, B. Self-assembled nitrogen-doped fullerenes and their catalysis for fuel cell and rechargeable metal-air battery applications. *Nanoscale* **2017**, *9*, 7373–7379. [[CrossRef](#)]

58. Lim, D.-H.; Lee, W.-J.; Wheldon, J.; Macy, N.L.; Smyrl, W.H. Electrochemical Characterization and Durability of Sputtered Pt Catalysts on TiO<sub>2</sub> Nanotube Arrays as a Cathode Material for PEFCs. *J. Electrochem. Soc.* **2010**, *157*, 535–541. [[CrossRef](#)]
59. Baskar, A.V.; Benzigar, M.R.; Talapaneni, S.N.; Singh, G.; Karakoti, A.S.; Yi, J.; Al-Muhtaseb, A.A.H.; Ariga, K.; Ajayan, P.M.; Vinu, A. Self-Assembled Fullerene Nanostructures: Synthesis and Applications. *Adv. Funct. Mater.* **2021**, *32*, 2106924. [[CrossRef](#)]
60. Basu, O.; Mukhopadhyay, S.; De, A.; Das, A.; Das, S.K. Tuning the electrochemical and catalytic ORR performance of C<sub>60</sub> by its encapsulation in ZIF-8: A solid-state analogue of dilute fullerene solution. *Mater. Chem. Front.* **2021**, *5*, 7654–7665. [[CrossRef](#)]
61. Saianand, G.; Gopalan, A.I.; Lee, J.C.; Sathish, C.I.; Gopalakrishnan, K.; Unni, G.E.; Shanbhag, D.; Dasireddy, V.; Yi, J.; Xi, S.; et al. Mixed Copper/Copper-Oxide Anchored Mesoporous Fullerene Nanohybrids as Superior Electrocatalysts toward Oxygen Reduction Reaction. *Small* **2020**, *16*, e1903937. [[CrossRef](#)] [[PubMed](#)]
62. Benzigar, M.R.; Joseph, S.; Saianand, G.; Gopalan, A.-I.; Sarkar, S.; Srinivasan, S.; Park, D.-H.; Kim, S.; Talapaneni, S.N.; Ramadass, K.; et al. Highly ordered iron oxide-mesoporous fullerene nanocomposites for oxygen reduction reaction and supercapacitor applications. *Microporous Mesoporous Mater.* **2019**, *285*, 21–31. [[CrossRef](#)]
63. Zhang, H.; Ma, Z.; Duan, J.; Liu, H.; Liu, G.; Wang, T.; Chang, K.; Li, M.; Shi, L.; Meng, X.; et al. Active Sites Implanted Carbon Cages in Core-Shell Architecture: Highly Active and Durable Electrocatalyst for Hydrogen Evolution Reaction. *ACS Nano* **2016**, *10*, 684–694. [[CrossRef](#)] [[PubMed](#)]
64. Peng, Y.; Chen, S. Electrocatalysts based on metal@carbon core@shell nanocomposites: An overview. *Green Energy Environ.* **2018**, *3*, 335–351. [[CrossRef](#)]
65. He, T.; Gao, G.; Kou, L.; Will, G.; Du, A. Endohedral metallofullerenes (M@C<sub>60</sub>) as efficient catalysts for highly active hydrogen evolution reaction. *J. Catal.* **2017**, *354*, 231–235. [[CrossRef](#)]
66. Chen, X.; Huang, S.; Zhang, H. Bimetallic alloys encapsulated in fullerenes as efficient oxygen reduction or oxygen evolution reaction catalysts: A density functional theory study. *J. Alloys Compd.* **2022**, *894*, 162508. [[CrossRef](#)]
67. Amiin, I.S.; Pu, Z.; Liu, X.; Owusu, K.A.; Monestel, H.G.R.; Boakye, F.O.; Zhang, H.; Mu, S. Multifunctional Mo-N/C@MoS<sub>2</sub> Electrocatalysts for HER, OER, ORR, and Zn-Air Batteries. *Adv. Funct. Mater.* **2017**, *27*, 1702300. [[CrossRef](#)]
68. An, C.-H.; Kang, W.; Deng, Q.-B.; Hu, N. Pt and Te codoped ultrathin MoS<sub>2</sub> nanosheets for enhanced hydrogen evolution reaction with wide pH range. *Rare Met.* **2021**, *41*, 378–384. [[CrossRef](#)]
69. Choi, Y.-H.; Lee, J.; Parija, A.; Cho, J.; Verkhoturov, S.V.; Al-Hashimi, M.; Fang, L.; Banerjee, S. An in Situ Sulfidation Approach for the Integration of MoS<sub>2</sub> Nanosheets on Carbon Fiber Paper and the Modulation of Its Electrocatalytic Activity by Interfacing with nC<sub>60</sub>. *ACS Catal.* **2016**, *6*, 6246–6254. [[CrossRef](#)]
70. Puente Santiago, A.R.; He, T.; Eraso, O.; Ahsan, M.A.; Nair, A.N.; Chava, V.S.N.; Zheng, T.; Pilla, S.; Fernandez-Delgado, O.; Du, A.; et al. Tailoring the Interfacial Interactions of van der Waals 1T-MoS<sub>2</sub>/C<sub>60</sub> Heterostructures for High-Performance Hydrogen Evolution Reaction Electrocatalysis. *J. Am. Chem. Soc.* **2020**, *142*, 17923–17927. [[CrossRef](#)]
71. Ahsan, M.A.; He, T.; Eid, K.; Abdullah, A.M.; Curry, M.L.; Du, A.; Puente Santiago, A.R.; Echegoyen, L.; Noveron, J.C. Tuning the Intermolecular Electron Transfer of Low-Dimensional and Metal-Free BCN/C<sub>60</sub> Electrocatalysts via Interfacial Defects for Efficient Hydrogen and Oxygen Electrochemistry. *J. Am. Chem. Soc.* **2021**, *143*, 1203–1215. [[CrossRef](#)] [[PubMed](#)]
72. Hasanzadeh, A.; Khataee, A.; Zarei, M.; Zhang, Y. Two-electron oxygen reduction on fullerene C<sub>60</sub>-carbon nanotubes covalent hybrid as a metal-free electrocatalyst. *Sci. Rep.* **2019**, *9*, 13780. [[CrossRef](#)] [[PubMed](#)]
73. Gao, R.; Dai, Q.; Du, F.; Yan, D.; Dai, L. C<sub>60</sub>-Adsorbed Single-Walled Carbon Nanotubes as Metal-Free, pH-Universal, and Multifunctional Catalysts for Oxygen Reduction, Oxygen Evolution, and Hydrogen Evolution. *J. Am. Chem. Soc.* **2019**, *141*, 11658–11666. [[CrossRef](#)] [[PubMed](#)]
74. Jiao, S.; Fu, X.; Wang, S.; Zhao, Y. Perfecting electrocatalysts via imperfections: Towards the large-scale deployment of water electrolysis technology. *Energy Environ. Sci.* **2021**, *14*, 1722–1770. [[CrossRef](#)]
75. Wu, G.; Santandreu, A.; Kellogg, W.; Gupta, S.; Ogoke, O.; Zhang, H.; Wang, H.-L.; Dai, L. Carbon nanocomposite catalysts for oxygen reduction and evolution reactions: From nitrogen doping to transition-metal addition. *Nano Energy* **2016**, *29*, 83–110. [[CrossRef](#)]
76. Huang, B.; Hou, K.; Liu, Y.; Hu, R.; Guan, L. Pre-fixing defects in carbon framework for revealing the active sites of oxygen reduction reaction at nitrogen-doped carbon nanotubes. *J. Energy Chem.* **2021**, *63*, 521–527. [[CrossRef](#)]
77. Ma, C.; Hou, P.; Wang, X.; Wang, Z.; Li, W.; Kang, P. Carbon nanotubes with rich pyridinic nitrogen for gas phase CO<sub>2</sub> electroreduction. *Appl. Catal. B* **2019**, *250*, 347–354. [[CrossRef](#)]
78. Zhang, A.; Jiang, S.; Zhou, M.; Cai, R.; Zhang, J. Effect of wall number on the electro-catalytic activity of nitrogen-doped carbon nanotubes for oxygen reduction reaction. *Chem. Ind. Eng. Prog.* **2022**, *41*, 2038–2045.
79. Cheng, Y.; Zhang, J.; Jiang, S.P. Are metal-free pristine carbon nanotubes electrocatalytically active? *Chem. Commun.* **2015**, *51*, 13764–13767. [[CrossRef](#)]
80. Guo, H.; Feng, Q.; Zhu, J.; Xu, J.; Li, Q.; Liu, S.; Xu, K.; Zhang, C.; Liu, T. Cobalt nanoparticle-embedded nitrogen-doped carbon/carbon nanotube frameworks derived from a metal-organic framework for tri-functional ORR, OER and HER electrocatalysis. *J. Mater. Chem. A* **2019**, *7*, 3664–3672. [[CrossRef](#)]
81. Yang, K.; Zaffran, J.; Yang, B. Fast prediction of oxygen reduction reaction activity on carbon nanotubes with a localized geometric descriptor. *Phys. Chem. Chem. Phys.* **2020**, *22*, 890–895. [[CrossRef](#)] [[PubMed](#)]
82. Li, Z.; Shao, M.; Yang, Q.; Tang, Y.; Wei, M.; Evans, D.G.; Duan, X. Directed synthesis of carbon nanotube arrays based on layered double hydroxides toward highly-efficient bifunctional oxygen electrocatalysis. *Nano Energy* **2017**, *37*, 98–107. [[CrossRef](#)]

83. Wu, M.; Zhang, G.; Chen, N.; Hu, Y.; Regier, T.; Rawach, D.; Sun, S. Self-Reconstruction of Co/Co<sub>2</sub>P Heterojunctions Confined in N-Doped Carbon Nanotubes for Zinc-Air Flow Batteries. *ACS Energy Lett.* **2021**, *6*, 1153–1161. [[CrossRef](#)]
84. Qu, K.; Zheng, Y.; Jiao, Y.; Zhang, X.; Dai, S.; Qiao, S. Polydopamine-Inspired, Dual Heteroatom-Doped Carbon Nanotubes for Highly Efficient Overall Water Splitting. *Adv. Energy Mater.* **2016**, *7*, 1602068. [[CrossRef](#)]
85. Liu, Z.; Yang, X.; Hu, G.; Feng, L. Ru Nanoclusters Coupled on Co/N-Doped Carbon Nanotubes Efficiently Catalyzed the Hydrogen Evolution Reaction. *ACS Sustain. Chem. Eng.* **2020**, *8*, 9136–9144. [[CrossRef](#)]
86. Tabassum, H.; Zou, R.; Mahmood, A.; Liang, Z.; Guo, S. A catalyst-free synthesis of B, N co-doped graphene nanostructures with tunable dimensions as highly efficient metal free dual electrocatalysts. *J. Mater. Chem. A* **2016**, *4*, 16469–16475. [[CrossRef](#)]
87. Han, X.; Zhang, W.; Ma, X.; Zhong, C.; Zhao, N.; Hu, W.; Deng, Y. Identifying the Activation of Bimetallic Sites in NiCo<sub>2</sub>S<sub>4</sub>@g-C<sub>3</sub>N<sub>4</sub>-CNT Hybrid Electrocatalysts for Synergistic Oxygen Reduction and Evolution. *Adv. Mater.* **2019**, *31*, 1808281. [[CrossRef](#)] [[PubMed](#)]
88. Li, X.; Fang, Y.; Li, F.; Tian, M.; Long, X.; Jin, J.; Ma, J. Ultrafine Co<sub>2</sub>P nanoparticles encapsulated in nitrogen and phosphorus dual-doped porous carbon nanosheet/carbon nanotube hybrids: High-performance bifunctional electrocatalysts for overall water splitting. *J. Mater. Chem. A* **2016**, *4*, 15501–15510. [[CrossRef](#)]
89. Feng, K.; Zheng, H.; Zhang, D.; Yuan, G.; Chang, L.-Y.; Chen, Y.; Zhong, J. Carbon nanotube supported PtO nanoparticles with hybrid chemical states for efficient hydrogen evolution. *J. Energy Chem.* **2021**, *58*, 364–369. [[CrossRef](#)]
90. Hu, X.; Li, Y.; Wei, X.; Wang, L.; She, H.; Huang, J.; Wang, Q. Preparation of double-layered Co–Ni/NiFeOOH co-catalyst for highly meliorated PEC performance in water splitting. *Adv. Powder Mater.* **2022**, *1*, 100024. [[CrossRef](#)]
91. Fang, B.; Yang, J.; Chen, C.; Zhang, C.; Chang, D.; Xu, H.; Gao, C. Carbon Nanotubes Loaded on Graphene Microfolds as Efficient Bifunctional Electrocatalysts for the Oxygen Reduction and Oxygen Evolution Reactions. *ChemCatChem* **2017**, *9*, 4520–4528. [[CrossRef](#)]
92. Wang, Q.; Wang, J.; Lei, Y.; Chen, Z.; Song, Y.; Luo, S. Research Progress on Carbon Nanotubes in Noble-Metal-Free Electrocatalytic Oxygen Reduction Reaction. *Chin. J. Inorg. Chem.* **2018**, *34*, 807–822.
93. Li, J.-S.; Wang, X.-R.; Li, J.-Y.; Zhang, S.; Sha, J.-Q.; Liu, G.-D.; Tang, B. Pomegranate-like molybdenum phosphide@phosphorus-doped carbon nanospheres coupled with carbon nanotubes for efficient hydrogen evolution reaction. *Carbon* **2018**, *139*, 234–240. [[CrossRef](#)]
94. Wu, M.; Zhang, G.; Qiao, J.; Chen, N.; Chen, W.; Sun, S. Ultra-long life rechargeable zinc-air battery based on high-performance trimetallic nitride and NCNT hybrid bifunctional electrocatalysts. *Nano Energy* **2019**, *61*, 86–95. [[CrossRef](#)]
95. Hou, Y.; Liang, Y.-L.; Shi, P.-C.; Huang, Y.-B.; Cao, R. Atomically dispersed Ni species on N-doped carbon nanotubes for electroreduction of CO<sub>2</sub> with nearly 100% CO selectivity. *Appl. Catal. B* **2020**, *271*, 118929. [[CrossRef](#)]
96. Hu, H.; Ou, J.; Xu, X.; Lin, Y.; Zhang, Y.; Zhao, H.; Chen, D.; He, M.; Huang, Y.; Deng, L. Graphene-assisted construction of electrocatalysts for carbon dioxide reduction. *Chem. Eng. J.* **2021**, *425*, 130587. [[CrossRef](#)]
97. Mazanek, V.; Luxa, J.; Matejkova, S.; Kucera, J.; Sedmidubsky, D.; Pumera, M.; Sofer, Z. Ultrapure Graphene Is a Poor Electrocatalyst: Definitive Proof of the Key Role of Metallic Impurities in Graphene-Based Electrocatalysis. *ACS Nano* **2019**, *13*, 1574–1582. [[CrossRef](#)]
98. Bie, C.; Yu, H.; Cheng, B.; Ho, W.; Fan, J.; Yu, J. Design, Fabrication, and Mechanism of Nitrogen-Doped Graphene-Based Photocatalyst. *Adv. Mater.* **2021**, *33*, 2003521. [[CrossRef](#)]
99. Shao, Y.; Jiang, Z.; Zhang, Q.; Guan, J. Progress in Nonmetal-Doped Graphene Electrocatalysts for the Oxygen Reduction Reaction. *ChemSusChem* **2019**, *12*, 2133–2146. [[CrossRef](#)]
100. Shiva Kumar, S.; Ramakrishna, S.U.B.; Rama Devi, B.; Himabindu, V. Phosphorus-doped graphene supported palladium (Pd/Pd) electrocatalyst for the hydrogen evolution reaction in PEM water electrolysis. *Int. J. Green Energy* **2018**, *15*, 558–567. [[CrossRef](#)]
101. Sanchez-Padilla, N.M.; Benavides, R.; Gallardo, C.; Fernandez, S.; De-Casas, E.; Morales-Acosta, D. Influence of doping level on the electrocatalytic properties for oxygen reduction reaction of N-doped reduced graphene oxide. *Int. J. Hydrogen Energy* **2021**, *46*, 26040–26052. [[CrossRef](#)]
102. Yan, P.; Liu, J.; Yuan, S.; Liu, Y.; Cen, W.; Chen, Y. The promotion effects of graphitic and pyridinic N combinational doping on graphene for ORR. *Appl. Surf. Sci.* **2018**, *445*, 398–403. [[CrossRef](#)]
103. Liu, A.; Guan, W.; Wu, K.; Ren, X.; Gao, L.; Ma, T. Density functional theory study of nitrogen-doped graphene as a high-performance electrocatalyst for CO<sub>2</sub>RR. *Appl. Surf. Sci.* **2021**, *540*, 148319. [[CrossRef](#)]
104. Wang, Y.; Sun, G.; Chen, L.; Du, Z.; Li, X.; Ye, C.; Liu, J.; Su, B. Engineering dual defective graphenes to synergistically improve electrocatalytic hydrogen evolution. *Appl. Surf. Sci.* **2021**, *566*, 150712. [[CrossRef](#)]
105. Li, S.; Ding, L.; Fan, L. Electrochemical synthesis of sulfur-doped graphene sheets for highly efficient oxygen reduction. *Sci. China Chem.* **2015**, *58*, 417–424. [[CrossRef](#)]
106. Sreekanth, N.; Nazrulla, M.A.; Vineesh, T.V.; Sailaja, K.; Phani, K.L. Metal-free boron-doped graphene for selective electroreduction of carbon dioxide to formic acid/formate. *Chem. Commun.* **2015**, *51*, 16061–16064. [[CrossRef](#)] [[PubMed](#)]
107. Xiao, Z.; Huang, X.; Xu, L.; Yan, D.; Huo, J.; Wang, S. Edge-selectively phosphorus-doped few-layer graphene as an efficient metal-free electrocatalyst for the oxygen evolution reaction. *Chem. Commun.* **2016**, *52*, 13008–13011. [[CrossRef](#)] [[PubMed](#)]
108. Liu, Z.; Ai, J.; Sun, M.; Han, F.; Li, Z.; Peng, Q.; Wang, Q.; Liu, J.; Liu, L. Phosphorous-Doped Graphite Layers with Outstanding Electrocatalytic Activities for the Oxygen and Hydrogen Evolution Reactions in Water Electrolysis. *Adv. Funct. Mater.* **2020**, *30*, 1910741. [[CrossRef](#)]

109. Li, F.; Shu, H.; Liu, X.; Shi, Z.; Liang, P.; Chen, X. Electrocatalytic Activity and Design Principles of Heteroatom-Doped Graphene Catalysts for Oxygen-Reduction Reaction. *J. Phys. Chem. C* **2017**, *121*, 14434–14442. [[CrossRef](#)]
110. Wang, Y.; Xiao, J.; Wang, H.; Zhang, T.; Yuan, S. Binary doping of nitrogen and phosphorus into porous carbon: A novel di-functional material for enhancing CO<sub>2</sub> capture and super-capacitance. *J. Mater. Sci. Technol.* **2022**, *99*, 73–81. [[CrossRef](#)]
111. Wu, M.; Liu, Y.; Zhu, Y.; Lin, J.; Liu, J.; Hu, H.; Wang, Y.; Zhao, Q.; Lv, R.; Qiu, J. Supramolecular polymerization-assisted synthesis of nitrogen and sulfur dual-doped porous graphene networks from petroleum coke as efficient metal-free electrocatalysts for the oxygen reduction reaction. *J. Mater. Chem. A* **2017**, *5*, 11331–11339. [[CrossRef](#)]
112. Zhang, X.; Wen, X.; Pan, C.; Xiang, X.; Hao, C.; Meng, Q.; Tian, Z.; Shen, P.; Jiang, S. N species tuning strategy in N, S co-doped graphene nanosheets for electrocatalytic activity and selectivity of oxygen redox reactions. *Chem. Eng. J.* **2022**, *431*, 133216. [[CrossRef](#)]
113. Liang, J.; Jiao, Y.; Jaroniec, M.; Qiao, S. Sulfur and nitrogen dual-doped mesoporous graphene electrocatalyst for oxygen reduction with synergistically enhanced performance. *Angew. Chem. Int. Ed.* **2012**, *51*, 11496–11500. [[CrossRef](#)] [[PubMed](#)]
114. Qin, Y.; Wu, H.; Zhang, L.; Zhou, X.; Bu, Y.; Zhang, W.; Chu, F.; Li, Y.; Kong, Y.; Zhang, Q.; et al. Aluminum and Nitrogen Codoped Graphene: Highly Active and Durable Electrocatalyst for Oxygen Reduction Reaction. *ACS Catal.* **2018**, *9*, 610–619. [[CrossRef](#)]
115. Razmjooei, F.; Singh, K.P.; Yang, D.-S.; Cui, W.; Jang, Y.; Yu, J.-S. Fe-Treated Heteroatom (S/N/B/P)-Doped Graphene Electrocatalysts for Water Oxidation. *ACS Catal.* **2017**, *7*, 2381–2391. [[CrossRef](#)]
116. Yang, R.; Xie, J.; Liu, Q.; Huang, Y.; Lv, J.; Ghausi, M.A.; Wang, X.; Peng, Z.; Wu, M.; Wang, Y. A trifunctional Ni-N/P-O-codoped graphene electrocatalyst enables dual-model rechargeable Zn–CO<sub>2</sub>/Zn–O<sub>2</sub> batteries. *J. Mater. Chem. A* **2019**, *7*, 2575–2580. [[CrossRef](#)]
117. Zhang, J.; Dai, L. Nitrogen, Phosphorus, and Fluorine Tri-doped Graphene as a Multifunctional Catalyst for Self-Powered Electrochemical Water Splitting. *Angew. Chem. Int. Ed.* **2016**, *55*, 13296–13300. [[CrossRef](#)]
118. Duan, X.; Xu, J.; Wei, Z.; Ma, J.; Guo, S.; Wang, S.; Liu, H.; Dou, S. Metal-Free Carbon Materials for CO<sub>2</sub> Electrochemical Reduction. *Adv. Mater.* **2017**, *29*, 1701784. [[CrossRef](#)]
119. Nemiwal, M.; Zhang, T.; Kumar, D. Graphene-based electrocatalysts: Hydrogen evolution reactions and overall water splitting. *Int. J. Hydrogen Energy* **2021**, *46*, 21401–21418. [[CrossRef](#)]
120. Ren, S.; Yu, Q.; Yu, X.; Rong, P.; Jiang, L.; Jiang, J. Graphene-supported metal single-atom catalysts: A concise review. *Sci. China Mater.* **2020**, *63*, 903–920. [[CrossRef](#)]
121. Zhang, Z.; Xiao, J.; Chen, X.; Yu, S.; Yu, L.; Si, R.; Wang, Y.; Wang, S.; Meng, X.; Wang, Y.; et al. Reaction Mechanisms of Well-Defined Metal-N<sub>4</sub> Sites in Electrocatalytic CO<sub>2</sub> Reduction. *Angew. Chem. Int. Ed.* **2018**, *57*, 16339–16342. [[CrossRef](#)] [[PubMed](#)]
122. Guan, E.; Ciston, J.; Bare, S.R.; Runnebaum, R.C.; Katz, A.; Kulkarni, A.; Kronawitter, C.X.; Gates, B.C. Supported Metal Pair-Site Catalysts. *ACS Catal.* **2020**, *10*, 9065–9085. [[CrossRef](#)]
123. Zhao, X.; Liu, X.; Huang, B.; Wang, P.; Pei, Y. Hydroxyl group modification improves the electrocatalytic ORR and OER activity of graphene supported single and bi-metal atomic catalysts (Ni, Co, and Fe). *J. Mater. Chem. A* **2019**, *7*, 24583–24593. [[CrossRef](#)]
124. Ren, M.; Guo, X.; Huang, S. Coordination-tuned Fe single-atom catalyst for efficient CO<sub>2</sub> electroreduction: The power of B atom. *Chem. Eng. J.* **2022**, *433*, 134270. [[CrossRef](#)]
125. Zhang, C.; Yang, S.; Wu, J.; Liu, M.; Yazdi, S.; Ren, M.; Sha, J.; Zhong, J.; Nie, K.; Jalilov, A.S.; et al. Electrochemical CO<sub>2</sub> Reduction with Atomic Iron-Dispersed on Nitrogen-Doped Graphene. *Adv. Energy Mater.* **2018**, *8*, 1703487. [[CrossRef](#)]
126. Li, X.; Chai, G.; Xu, X.; Liu, J.; Zhong, Z.; Cao, A.; Tao, Z.; You, W.; Kang, L. Electrocatalytic reduction of CO<sub>2</sub> to CO over iron phthalocyanine-modified graphene nanocomposites. *Carbon* **2020**, *167*, 658–667. [[CrossRef](#)]
127. Huang, P.; Cheng, M.; Zhang, H.; Zuo, M.; Xiao, C.; Xie, Y. Single Mo atom realized enhanced CO<sub>2</sub> electro-reduction into formate on N-doped graphene. *Nano Energy* **2019**, *61*, 428–434. [[CrossRef](#)]
128. Jiang, K.; Siahrostami, S.; Zheng, T.; Hu, Y.; Hwang, S.; Stavitski, E.; Peng, Y.; Dynes, J.; Gangisetty, M.; Su, D.; et al. Isolated Ni single atoms in graphene nanosheets for high-performance CO<sub>2</sub> reduction. *Energy Environ. Sci.* **2018**, *11*, 893–903. [[CrossRef](#)]
129. Qiu, H.; Du, P.; Hu, K.; Gao, J.; Li, H.; Liu, P.; Ina, T.; Ohara, K.; Ito, Y.; Chen, M. Metal and Nonmetal Codoped 3D Nanoporous Graphene for Efficient Bifunctional Electrocatalysis and Rechargeable Zn–Air Batteries. *Adv. Mater.* **2019**, *31*, 1900843. [[CrossRef](#)]
130. Liu, L.; Corma, A. Metal Catalysts for Heterogeneous Catalysis: From Single Atoms to Nanoclusters and Nanoparticles. *Chem. Rev.* **2018**, *118*, 4981–5079. [[CrossRef](#)]
131. Pang, L.; Miao, Y.; Bhange, S.N.; Barras, A.; Addad, A.; Roussel, P.; Amin, M.A.; Kurungot, S.; Szunerits, S.; Boukherroub, R. Enhanced electrocatalytic activity of PtRu/nitrogen and sulphur co-doped crumbled graphene in acid and alkaline media. *J. Colloid Interface Sci.* **2021**, *590*, 154–163. [[CrossRef](#)] [[PubMed](#)]
132. Barman, B.K.; Sarkar, B.; Nanda, K.K. Pd-coated Ru nanocrystals supported on N-doped graphene as HER and ORR electrocatalysts. *Chem. Commun.* **2019**, *55*, 13928–13931. [[CrossRef](#)] [[PubMed](#)]
133. Wang, Q.; Xu, C.; Liu, W.; Hung, S.; Bin Yang, H.; Gao, J.; Cai, W.; Chen, H.; Li, J.; Liu, B. Coordination engineering of iridium nanocluster bifunctional electrocatalyst for highly efficient and pH-universal overall water splitting. *Nat. Commun.* **2020**, *11*, 4246. [[CrossRef](#)]
134. Huang, J.; Guo, X.; Yue, G.; Hu, Q.; Wang, L. Boosting CH<sub>3</sub>OH Production in Electrocatalytic CO<sub>2</sub> Reduction over Partially Oxidized 5 nm Cobalt Nanoparticles Dispersed on Single-Layer Nitrogen-Doped Graphene. *ACS Appl. Mater. Interfaces* **2018**, *10*, 44403–44414. [[CrossRef](#)] [[PubMed](#)]

135. Zhang, G.; Wang, P.; Lu, W.; Wang, C.; Li, Y.; Ding, C.; Gu, J.; Zheng, X.; Cao, F. Co Nanoparticles/Co, N, S Tri-doped Graphene Templated from In-Situ-Formed Co, S Co-doped g-C<sub>3</sub>N<sub>4</sub> as an Active Bifunctional Electrocatalyst for Overall Water Splitting. *ACS Appl. Mater. Interfaces* **2017**, *9*, 28566–28576. [[CrossRef](#)] [[PubMed](#)]
136. Phan, T.H.; Banjac, K.; Cometto, F.P.; Dattila, F.; Garcia-Muelas, R.; Raaijman, S.J.; Ye, C.; Koper, M.T.M.; Lopez, N.; Lingensfelder, M. Emergence of Potential-Controlled Cu-Nanocuboids and Graphene-Covered Cu-Nanocuboids under Operando CO<sub>2</sub> Electroreduction. *Nano Lett.* **2021**, *21*, 2059–2065. [[CrossRef](#)]
137. Bonnefont, A.; Ryabova, A.S.; Schott, T.; Kéranguéven, G.; Istomin, S.Y.; Antipov, E.V.; Savinova, E.R. Challenges in the understanding oxygen reduction electrocatalysis on transition metal oxides. *Curr. Opin. Electrochem.* **2019**, *14*, 23–31. [[CrossRef](#)]
138. Gu, X.K.; Carneiro, J.S.A.; Samira, S.; Das, A.; Ariyasingha, N.M.; Nikolla, E. Efficient Oxygen Electrocatalysis by Nanostructured Mixed-Metal Oxides. *J. Am. Chem. Soc.* **2018**, *140*, 8128–8137. [[CrossRef](#)]
139. Tian, Y.; Xu, L.; Li, M.; Yuan, D.; Liu, X.; Qian, J.; Dou, Y.; Qiu, J.; Zhang, S. Interface Engineering of CoS/CoO@N-Doped Graphene Nanocomposite for High-Performance Rechargeable Zn-Air Batteries. *Nano-Micro Lett.* **2020**, *13*, 35–49.
140. Wu, F.; Niu, Y.; Huang, X.; Mei, Y.; Wu, X.; Zhong, C.; Hu, W. Manganese/Cobalt Bimetal Nanoparticles Encapsulated in Nitrogen-Rich Graphene Sheets for Efficient Oxygen Reduction Reaction Electrocatalysis. *ACS Sustain. Chem. Eng.* **2018**, *6*, 10545–10551. [[CrossRef](#)]
141. Zhang, B.; Guo, Z.; Zuo, Z.; Pan, W.; Zhang, J. The ensemble effect of nitrogen doping and ultrasmall SnO<sub>2</sub> nanocrystals on graphene sheets for efficient electroreduction of carbon dioxide. *Appl. Catal. B* **2018**, *239*, 441–449. [[CrossRef](#)]
142. Maiti, K.; Kim, K.; Noh, K.-J.; Han, J.W. Synergistic coupling ensuing cobalt phosphosulfide encapsulated by heteroatom-doped two-dimensional graphene shell as an excellent catalyst for oxygen electroreduction. *Chem. Eng. J.* **2021**, *423*, 130233. [[CrossRef](#)]
143. Lai, C.; Gong, M.; Zhou, Y.; Fang, J.; Huang, L.; Deng, Z.; Liu, X.; Zhao, T.; Lin, R.; Wang, K.; et al. Sulphur modulated Ni<sub>3</sub>FeN supported on N/S co-doped graphene boosts rechargeable/flexible Zn-air battery performance. *Appl. Catal. B* **2020**, *274*, 119086. [[CrossRef](#)]
144. Hegazy, M.B.Z.; Berber, M.R.; Yamauchi, Y.; Pakdel, A.; Cao, R.; Apfel, U.P. Synergistic Electrocatalytic Hydrogen Evolution in Ni/NiS Nanoparticles Wrapped in Multi-Heteroatom-Doped Reduced Graphene Oxide Nanosheets. *ACS Appl. Mater. Interfaces* **2021**, *13*, 34043–34052. [[CrossRef](#)] [[PubMed](#)]
145. Arunkumar, P.; Gayathri, S.; Han, J.H. A Complementary Co-Ni Phosphide/Bimetallic Alloy-Interspersed N-Doped Graphene Electrocatalyst for Overall Alkaline Water Splitting. *ACS Appl. Mater. Interfaces* **2021**, *14*, 1921–1935. [[CrossRef](#)]
146. Liu, S.; Cheng, L.; Li, K.; Yin, C.; Tang, H.; Wang, Y.; Wu, Z. RuN<sub>4</sub> Doped Graphene Oxide, a Highly Efficient Bifunctional Catalyst for Oxygen Reduction and CO<sub>2</sub> Reduction from Computational Study. *ACS Sustain. Chem. Eng.* **2019**, *7*, 8136–8144. [[CrossRef](#)]
147. Guo, D.; Zeng, Z.; Wan, Z.; Li, Y.; Xi, B.; Wang, C. A CoN-based OER Electrocatalyst Capable in Neutral Medium: Atomic Layer Deposition as Rational Strategy for Fabrication. *Adv. Funct. Mater.* **2021**, *31*, 2101324. [[CrossRef](#)]
148. Zhang, M.; Xu, Y.; Zhang, H.; Duan, Z.; Ren, T.; Wang, Z.; Li, X.; Wang, L.; Wang, H. Synergistic coupling of P-doped Pd<sub>4</sub>S nanoparticles with P/S-co-doped reduced graphene oxide for enhanced alkaline oxygen reduction. *Chem. Eng. J.* **2022**, *429*, 132194. [[CrossRef](#)]
149. Yan, Y.; Gong, J.; Chen, J.; Zeng, Z.; Huang, W.; Pu, K.; Liu, J.; Chen, P. Recent Advances on Graphene Quantum Dots: From Chemistry and Physics to Applications. *Adv. Mater.* **2019**, *31*, 1808283. [[CrossRef](#)]
150. Yu, J.; Song, H.; Li, X.; Tang, L.; Tang, Z.; Yang, B.; Lu, S. Computational Studies on Carbon Dots Electrocatalysis: A Review. *Adv. Funct. Mater.* **2021**, *31*, 2107196. [[CrossRef](#)]
151. Zhai, Y.; Zhang, B.; Shi, R.; Zhang, S.; Liu, Y.; Wang, B.; Zhang, K.; Waterhouse, G.I.N.; Zhang, T.; Lu, S. Carbon Dots as New Building Blocks for Electrochemical Energy Storage and Electrocatalysis. *Adv. Energy Mater.* **2021**, *12*, 2103426. [[CrossRef](#)]
152. Ali, M.; Riaz, R.; Anjum, A.S.; Sun, K.C.; Li, H.; Jeong, S.H.; Ko, M.J. Graphene quantum dots induced porous orientation of holey graphene nanosheets for improved electrocatalytic activity. *Carbon* **2021**, *171*, 493–506. [[CrossRef](#)]
153. Xia, C.; Qiu, Y.; Xia, Y.; Zhu, P.; King, G.; Zhang, X.; Wu, Z.; Kim, J.Y.T.; Cullen, D.A.; Zheng, D.; et al. General synthesis of single-atom catalysts with high metal loading using graphene quantum dots. *Nat. Chem.* **2021**, *13*, 887–894. [[CrossRef](#)] [[PubMed](#)]
154. Van Tam, T.; Kang, S.G.; Babu, K.F.; Oh, E.-S.; Lee, S.G.; Choi, W.M. Synthesis of B-doped graphene quantum dots as a metal-free electrocatalyst for the oxygen reduction reaction. *J. Mater. Chem. A* **2017**, *5*, 10537–10543. [[CrossRef](#)]
155. Guo, Q.; Feng, J.; Chen, D.; Song, N.; Dong, H.; Yu, L.; Dong, L. Theoretical Insights into Enhanced Electrocatalytic Activity of Oxygen Reduction Reactions on N/S-Codoped Graphene Quantum Dots. *J. Phys. Chem. C* **2021**, *125*, 9747–9755. [[CrossRef](#)]
156. Zheng, D.; Yu, L.; Liu, W.; Dai, X.; Niu, X.; Fu, W.; Shi, W.; Wu, F.; Cao, X. Structural advantages and enhancement strategies of heterostructure water-splitting electrocatalysts. *Cell Rep. Phys. Sci.* **2021**, *2*, 100443. [[CrossRef](#)]
157. Yan, Y.; Zhai, D.; Liu, Y.; Gong, J.; Chen, J.; Zan, P.; Zeng, Z.; Li, S.; Huang, W.; Chen, P. van der Waals Heterojunction between a Bottom-Up Grown Doped Graphene Quantum Dot and Graphene for Photoelectrochemical Water Splitting. *ACS Nano* **2020**, *14*, 1185–1195. [[CrossRef](#)]
158. Gong, J.; Zhang, Z.; Zeng, Z.; Wang, W.; Kong, L.; Liu, J.; Chen, P. Graphene quantum dots assisted exfoliation of atomically-thin 2D materials and as-formed 0D/2D van der Waals heterojunction for HER. *Carbon* **2021**, *184*, 554–561. [[CrossRef](#)]
159. Zhang, Z.; Xu, D.; Li, J.; Liu, J.; Long, X.; Su, K.; Guo, J.; Tong, H.; Liu, Z.; Qian, D. Highly electrocatalytic performance of bimetallic Co-Fe sulfide nanoparticles encapsulated in N-doped carbon nanotubes on reduced graphene oxide for oxygen evolution. *J. Alloys Compd.* **2021**, *881*, 160667. [[CrossRef](#)]

160. Zhao, J.; Liu, Y.; Quan, X.; Chen, S.; Zhao, H.; Yu, H. Nitrogen and sulfur co-doped graphene/carbon nanotube as metal-free electrocatalyst for oxygen evolution reaction: The enhanced performance by sulfur doping. *Electrochim. Acta* **2016**, *204*, 169–175. [[CrossRef](#)]
161. Sun, J.; Lowe, S.E.; Zhang, L.; Wang, Y.; Pang, K.; Wang, Y.; Zhong, Y.; Liu, P.; Zhao, K.; Tang, Z.; et al. Ultrathin Nitrogen-Doped Holey Carbon@Graphene Bifunctional Electrocatalyst for Oxygen Reduction and Evolution Reactions in Alkaline and Acidic Media. *Angew. Chem. Int. Ed.* **2018**, *57*, 16511–16515. [[CrossRef](#)]
162. Li, S.; Yu, Z.; Yang, Y.; Liu, Y.; Zou, H.; Yang, H.; Jin, J.; Ma, J. Nitrogen-doped truncated carbon nanotubes inserted into nitrogen-doped graphene nanosheets with a sandwich structure: A highly efficient metal-free catalyst for the HER. *J. Mater. Chem. A* **2017**, *5*, 6405–6410. [[CrossRef](#)]
163. Tong, X.; Cherif, M.; Zhang, G.; Zhan, X.; Ma, J.; Almesrati, A.; Vidal, F.; Song, Y.; Claverie, J.P.; Sun, S. N, P-Codoped Graphene Dots Supported on N-Doped 3D Graphene as Metal-Free Catalysts for Oxygen Reduction. *ACS Appl. Mater. Interfaces* **2021**, *13*, 30512–30523. [[CrossRef](#)] [[PubMed](#)]
164. Guo, X.; Duan, X.; Ji, J.; Fan, X.; Li, Y.; Zhang, F.; Zhang, G.; Zhu, Y.; Peng, W.; Wang, S. Synthesis of nitrogen and sulfur doped graphene on graphite foam for electro-catalytic phenol degradation and water splitting. *J. Colloid Interface Sci.* **2021**, *583*, 139–148. [[CrossRef](#)] [[PubMed](#)]
165. Yang, J.; Sun, H.; Liang, H.; Ji, H.; Song, L.; Gao, C.; Xu, H. A Highly Efficient Metal-Free Oxygen Reduction Electrocatalyst Assembled from Carbon Nanotubes and Graphene. *Adv. Mater.* **2016**, *28*, 4606–4613. [[CrossRef](#)] [[PubMed](#)]
166. Tavakkoli, M.; Flahaut, E.; Peljo, P.; Sainio, J.; Davodi, F.; Lobiak, E.V.; Mustonen, K.; Kauppinen, E.I. Mesoporous Single-Atom-Doped Graphene–Carbon Nanotube Hybrid: Synthesis and Tunable Electrocatalytic Activity for Oxygen Evolution and Reduction Reactions. *ACS Catal.* **2020**, *10*, 4647–4658. [[CrossRef](#)]
167. Lai, C.; Wang, J.; Lei, W.; Xuan, C.; Xiao, W.; Zhao, T.; Huang, T.; Chen, L.; Zhu, Y.; Wang, D. Restricting Growth of Ni<sub>3</sub>Fe Nanoparticles on Heteroatom-Doped Carbon Nanotube/Graphene Nanosheets as Air-Electrode Electrocatalyst for Zn-Air Battery. *ACS Appl. Mater. Interfaces* **2018**, *10*, 38093–38100. [[CrossRef](#)]